

# **Effect of change in strain path during cold rolling on the evolution of microstructure, texture and hardness properties of different Aluminum alloys**

*Dissertation submitted in partial fulfillment of the requirements for the award of the degree of*

*Master of Technology*

Submitted by

**Saptarshi Saha**

**MS10M01**

Under the guidance of

**Dr. Pinaki Prasad Bhattacharjee**



भारतीय प्रौद्योगिकी संस्थान हैदराबाद  
Indian Institute of Technology Hyderabad

**Department of Materials Science & Engineering**

**Indian Institute of Technology, Hyderabad**

**2012**

## Declaration

I declare that this written submission represents my ideas in my own words, and where others' ideas or words have been included, I have adequately cited and referenced the original sources. I also declare that I have adhered to all principles of academic honesty and integrity and have not misrepresented or fabricated or falsified any idea/data/fact/source in my submission. I understand that any violation of the above will be a cause for disciplinary action by the Institute and can also evoke penal action from the sources that have thus not been properly cited, or from whom proper permission has not been taken when needed.



(Signature)

---

SAPTARSHI SAHA

(– Student Name –)

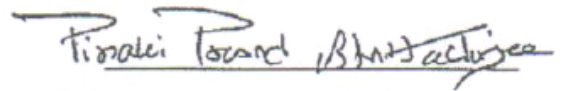
---

MS10M001

(-Roll No-)

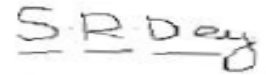
# Dissertation Approval Sheet

Dissertation titled “**Effect of change in strain path during cold rolling on the evolution of microstructure, texture and hardness properties of different Aluminum alloys**” submitted by Saptarshi Saha is approved for the award of degree of **Master of Technology**.



Dr. Pinaki Prasad Bhattacharjee (Department of Materials Science and Engineering)

Advisor



Dr. Suhas Ranjan Dey (Department of Materials Science and Engineering)

Examiner



Dr. R. Ranjith (Department of Materials Science and Engineering)

Examiner



Dr. Raja Banerjee (Department of Mechanical Engineering)

Chairman

## Acknowledgement

First of all, I would like to express my deep sense of gratitude to my project guide **Dr. Pinaki Prasad Bhattacharjee**, for his esteemed guidance. He has been a role model for me and influences me in almost every aspect. His guidance and motivation helped me a lot during my post-graduate study.

I would like to thank Professor **Indradev Samajdar**, IIT Bombay, for his kind permission to carry out the XRD and EBSD characterization work, valuable guidance and assistance during my visit to IIT Bombay for experimental work. I would like to thank **Professor N. Tsuji**, Kyoto University, Japan for his kind permission to carry out the rolling of the specimens in his laboratory.

I would also like to thank Partha and Nasim for helping me during my experimental work at IIT Bombay. Thanks are due to PhD scholar Jagga Rao Gatti for helping me selflessly whenever I needed it the most. It has been always very comfortable to share any kind of problem with him.

I would also like to thank all my friends; Mohit Joshi, Vijay Prakash, Sajin George and Palli Srinivas for their kind support and encouragement extended throughout the project work. We had a great time together.

Last but not the least; I would like to express my sincere thanks to all others who have directly or indirectly helped me in my project work.

## Abstract

The effect of strain path change during heavy cold rolling on the development of texture, microstructure and hardness properties is investigated in different aluminum alloys. For this purpose 99.99% aluminum (4N-Al) and Al-2.5%Mg alloy was deformed up to 90% reduction in thickness by two different rolling routes, namely, unidirectional cold rolling (UCR) and cross cold rolling (CCR). In the CCR route the specimens are rotated by 90° around the normal direction (ND) so that the transverse direction (TD) of the previous pass became the rolling direction (RD) of the present pass. The evolution of microstructure, texture was subsequently studied by X-ray and electron back scatter diffraction (XRD and EBSD, respectively).

Evolution of a lamellar type deformation microstructure is observed in all materials irrespective of the processing route. The UCR processed 4N-Al shows much pronounced dynamic recovery as compared to the CCR processed materials the reasons for which need to be investigated further. In sharp contrast, the CCR processing does not affect the microstructural development of Al-Mg alloy significantly as established by the values of the various structural parameters of differently processed heavily deformed materials. This seems to originate from the much restricted dynamic recovery in Al-Mg alloy due to the presence of Mg as solute.

UCR processing leads to a pure metal type deformation texture characterized by strong Cu ( $\{112\}\langle 111\rangle$ ), S ( $\{123\}\langle 634\rangle$ ) and  $B_S$  ( $\{110\}\langle 112\rangle$ ) components in 4N-Al and Al-Mg alloys. However, Al-Mg alloy develops a much stronger  $B_S$  component after CCR processing than its UCR processed counterpart. In contrast, in CCR processed texture of 4N-Al,  $B_S$  and  $B_S^{ND}$  ( $(011)[17\ -13\ 13]$ ) components are observed. The combined volume fraction of these two components is, however, much smaller than the volume fraction of the  $B_S$  component in Al-Mg.

The hardness values of heavily deformed Al-Mg processed by different routes do not differ appreciably which is consistent with the very similar values of their microstructural parameters. In contrast, the CCR processed 4N-Al show consistently higher values than its UCR processed counterpart presumably due to less dynamic recovery in the former material. Importantly, CCR processing appears to have more pronounced effect on microstructure, texture and properties of materials with strong tendency for dynamic recovery.

# Nomenclature

UCR- Unidirectional Cold Rolling

CCR- Cross Cold Rolling

SCR- Straight Cold Rolling

GO map- Grain Orientation map

GB map- Grain Boundary map

ODF- Orientation Distribution Function

PF- Pole Figure

FCC- Face Centered Cubic

SFE- Stacking Fault Energy

RD- Rolling Direction

TD- Transverse Direction

ND- Normal Direction

HAGB- High Angle Grain Boundary

LAGB- Low Angle Grain Boundary

XRD- X-Ray Diffraction

EBSD- Electron Back Scattered Diffraction

# Contents

Declaration.....	ii
Approval Sheet.....	iii
Acknowledgements.....	iv
Abstract.....	v
<b>Nomenclature.....</b>	<b>vi</b>
<b>1 Introduction</b>	
1.1 Objective & scope of present work.....	2
<b>2 Literature Review.....</b>	<b>3</b>
<b>3 Experimental Procedure</b>	
3.1 Processing of materials.....	6
3.2 Characterization .....	8
3.3 Hardness test.....	9
<b>4 Experimental Results</b>	
4.1 4N Aluminum.....	10
4.1.1 Microstructure and texture of starting material.....	10
4.1.2 Deformation by unidirectional cold rolling (UCR).....	11
4.1.3 Deformation by cross cold rolling (CCR).....	20
4.1.4 Evolution of hardness property.....	29
4.2 Al-2.5Mg alloy.....	30
4.2.1 Microstructure and texture of starting material.....	30
4.2.2 Deformation by unidirectional cold rolling (UCR).....	31
4.2.3 Deformation by cross cold rolling (CCR).....	40
4.2.4 Evolution of hardness property.....	49
<b>5 Discussions</b>	
5.1 Effect of CCR processing on texture evolution.....	50
5.2 Effect of CCR processing on microstructure evolution.....	53

5.3	Evolution of hardness properties.....	56
5.4	Future work.....	56
<b>6</b>	<b>Summary &amp; Conclusions.....</b>	<b>57</b>
<b>7</b>	<b>References.....</b>	<b>59</b>



# Chapter 1

## Introduction

Aluminum alloys are extensively used in modern automobile and aircraft industries due to their lightweight combined with many attractive mechanical properties. Deformation processing constitutes an important step in the overall manufacturing cycle to achieve the desired mechanical properties in these materials. Deformation processing of sheet materials leads to significant changes in microstructure and crystallographic texture which in turn greatly affect the mechanical properties. Therefore, microstructure and texture constitute two key aspects of deformation processing and are energetically studied for optimizing the properties of structural materials [1-4]. The development of characteristic microstructures and textures depends upon processing parameters such as temperature, strain, strain-rate and strain path. Amongst several parameters listed above, in case of metals and alloys, the strain path change has important effects on the evolution of microstructure and texture [5-7] and as a consequence can significantly affect the end properties of materials.

The change in strain path under rolling geometry can be implemented by changing the rolling direction (RD) between consecutive passes by rotating the sample about the normal direction (ND) in a multi-pass rolling process as shown schematically in Fig.1.1.

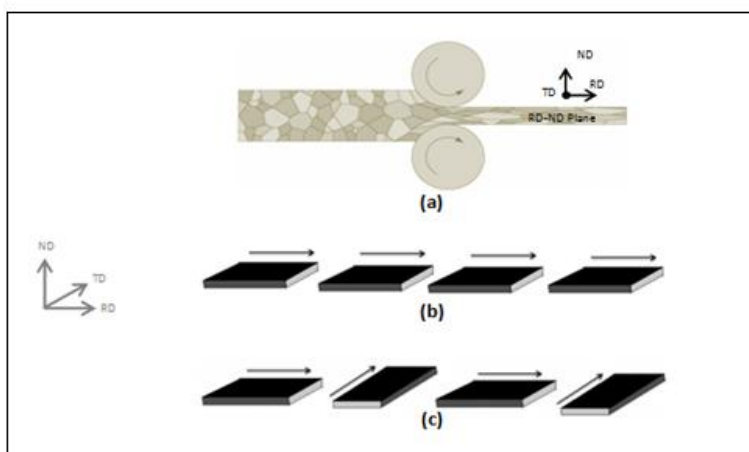


Fig. 1.1: (a) Rolling process with reference directions as RD- Rolling Direction, ND-Normal Direction and TD-Transverse Direction; (b) unidirectional cold rolling (UCR) and (c) cross cold rolling (CCR) routes.

This process has been termed as cross cold rolling (CCR)[8]. It is presumed that CCR leads to the destabilization of the substructure of the previous rolling pass resulting in substantial changes in the formation of deformation texture.

## **1.1 Objectives and scope of the present work**

The objective of the present work is to understand the evolution of microstructure, texture and mechanical properties in high purity aluminum (99.99% also referred to as 4N-Al) and Al-2.5%Mg alloy. The two experimental materials have vastly different strength and dynamic recovery behavior. Although, the effect of CCR processing has been investigated in different aluminum alloys [9-14], no systematic studies have been carried out so far to study the effect of cross rolling on the development of microstructure and texture in materials with varying dynamic recovery properties. The motivation for the present study is to clarify these unresolved issues.

# Chapter 2

## Literature Review

Microstructure and texture evolution in fcc metals and alloys during deformation processing has been a subject of much interest and substantial effort has been made in understanding these issues[1-3,15]. Development of a lamellar type structure during heavy cold rolling of fcc materials has frequently been reported accompanied by characteristic changes in crystallographic texture[16-20]. The simplest description of cold rolling texture in FCC metals would be the presence of two incomplete fibers, namely, the  $\alpha$  and  $\beta$ -fibers as shown in Fig. 2.1. The  $\alpha$ -fiber extends from the Goss orientation ( $\{110\} \langle 001 \rangle$ ) to the Brass ( $B_S$ ) orientation ( $\{110\} \langle 112 \rangle$ ) and the  $\beta$ -fiber which extends from the copper orientation (Cu component;  $\{112\} \langle 111 \rangle$ ) to the  $B_S$  orientation through the S-orientation ( $\{123\} \langle 634 \rangle$ )[2]. In high to medium stacking fault energy (SFE) FCC materials like Al, Ni and Cu the cold rolling texture is described as ‘pure metal’ or ‘copper type’ texture which is characterized by strong presence of the Cu, S and  $B_S$  components whereas in low SFE materials (such as austenitic stainless steel) the cold rolling texture is ‘alloy type’ characterized by the presence of strong  $B_S$  component[21]. However, the processing parameters such as temperature, strain and strain-rate can greatly affect the formation of deformation microstructure and texture and departure for the above simplistic description of texture is frequently reported.

Amongst several processing parameters strain path change has been found to greatly affect the formation of microstructure and texture. The strain path change during cold rolling can be achieved by cross cold rolling or CCR as already introduced in chapter 1. It is presumed that during CCR processing the substructure of the previous rolling pass is rotated by  $90^\circ$  which make stable orientations and substructure of previous pass unstable along new rolling direction resulting in substantial difference in the microstructure and texture evolution.

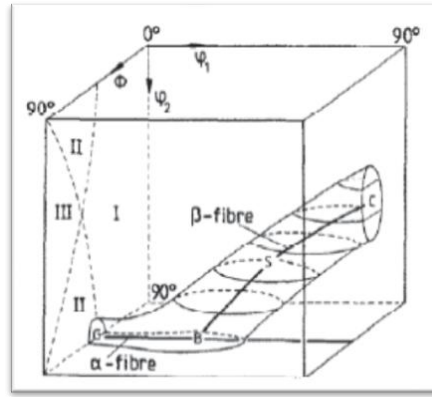


Fig.2.1: Schematic representation of the  $\alpha$  and  $\beta$  fibers in the Euler space[2].

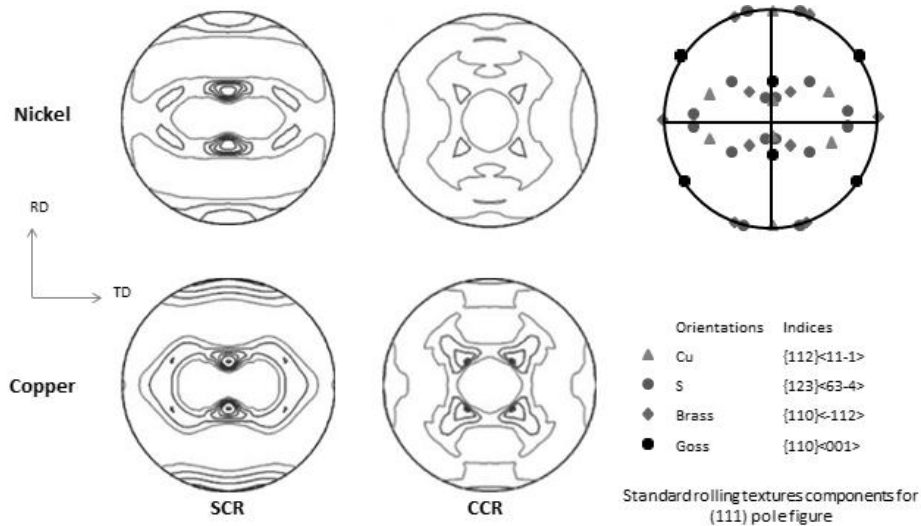


Fig.2.2:- (111) pole figures of nickel and copper deformed by UCR and CCR routes[22].

The formation of texture during CCR has been studied experimentally and through modeling in different fcc metals and alloys. Experimental results obtained in fcc nickel, copper and copper alloys indicate the development of strong brass and rotated brass components in CCR processed materials as compared to their UCR processed counterparts[6,22,23]. This fact is clearly illustrated in Fig. 2.2 which shows the (111) pole figure (PF) of UCR and CCR processed Ni and Cu. Comparison of the PFs clearly reveals the development of strong  $B_S$  component in CCR processed materials. Bocker et al have also reported the development of a strong  $B_S$  component in an Al-Mn alloy after heavy deformation (~93% reduction in thickness) by CCR processing as may be seen from the  $\phi_2=0^\circ$  and  $\phi_2=45^\circ$  section in the complete ODF shown in Fig.2.3[9].

It has been argued that change in strain path results in rotation and destabilization of substructure which results in microstructural and textural changes. The theoretical analysis by Hong et al[7] in terms of rotation field and divergence of rotation field predict that amongst different texture components the  $\{011\}\langle 1-11 \rangle$  (which is basically ND rotated  $B_S$  orientation) would be stable under cross-rolling due to its higher inverse rotation rate and large negative divergence. The grains with orientations along the  $\alpha$ -fiber will rotate to the  $B_S$  orientation (stable orientation during unidirectional rolling) and then will further rotate away to the  $\{011\}\langle 1\bar{1}1 \rangle$  orientation when the direction of rolling is changed by  $90^\circ$  around the ND, thus, oscillating between the  $B_S$  and rotated brass orientation  $\{011\}\langle 1-11 \rangle$  which would be the two stable end orientations in CCR.

The present work makes an attempt to study the development of microstructure and texture in 4N-Al and Al-2.5%Mg alloy with widely different recovery behavior. The brief yet critical literature review on the proposed area indicates that no systematic study has been conducted to understand the effect of CCR on microstructural and textural evolution in materials with vastly different dynamic recovery behavior or in other words, materials which are known to develop different substructures during conventional deformation processing. The present work attempts to fill in this knowledge gap.

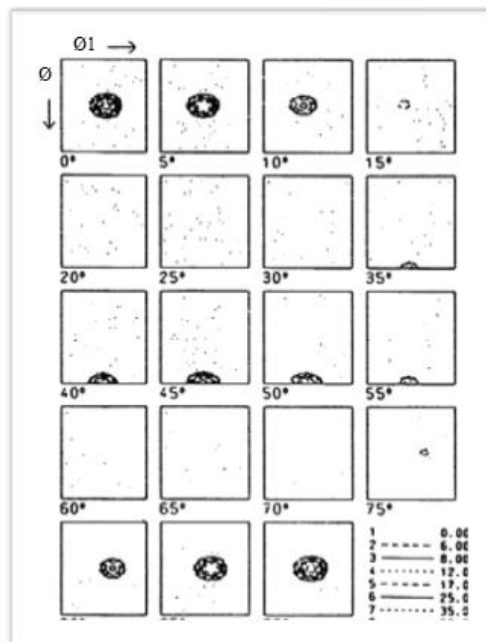


Fig. 2.3: ODF of 93% multi-pass cross rolled Al-Mn alloy showing strong  $B_S$  component [9].

# Chapter 3

## Experimental Procedure

### 3.1 Processing of materials

In the present work Al-2.5Mg (As cast) samples having dimensions ( $\sim 160\text{mm}^L \times 60\text{mm}^W \times 10\text{mm}^T$ ) were deformed up to 80% reduction in thickness by multi pass cold rolling followed by annealing at  $400^\circ$  for 1 hr in an air furnace and were used as the starting material for further rolling (as shown in Fig. 3.1). In case of 99.99% pure aluminum as-received materials in the annealed condition were used for further rolling. The fully recrystallized Al-2.5 Mg alloy and 4N Al were multi-pass cold rolled up to 20%, 40%, 60% and 90% thickness reduction in thickness using the UCR and CCR routes (as described previously) using a laboratory scale rolling mill with oil lubricated rolls. The complete processing cycle is summarized in Fig.3.2.

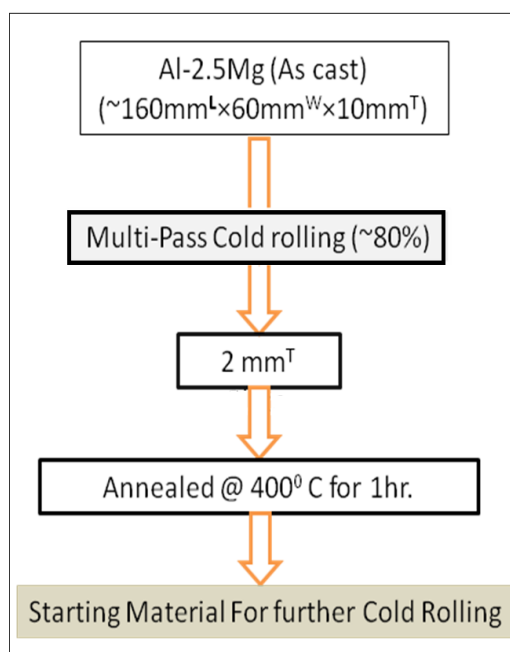


Fig.3.1: Preparation of as-received Al-Mg alloy for further cold rolling

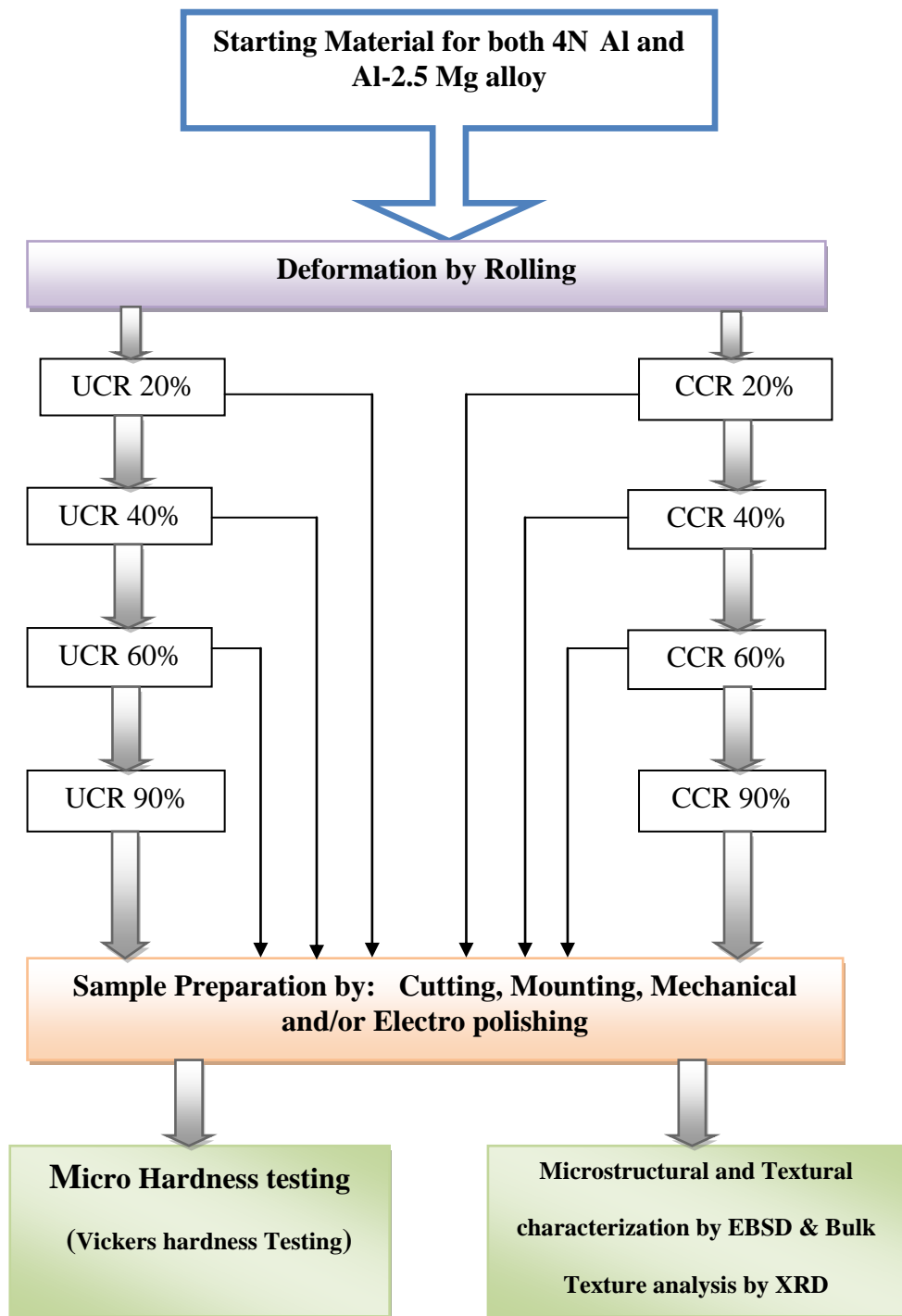


Fig.3.2: Process Chart of complete Experimental work

## 3.2 Characterization

Sample preparation was one of the major parts of the experimental procedure. 20%, 40% and 60% deformed samples are cut into pieces using Secotom-15 (Struers, Denmark) precession cutter, where as 90 % deformed samples are sectioned using Minitom (diamond cutter, Struers). For hardness measurement small piece of samples were mounted (Fig.3.3) using Citopress -10 and then they are polished on a series of 100, 180 and 500 of emery papers. The polished samples were finally diamond polished using colloidal silica.

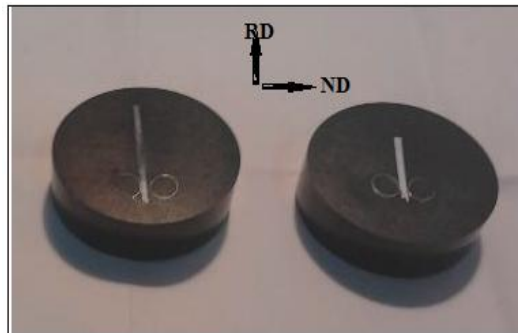


Fig. 3.3: Samples in the mounted condition

Samples for EBSD measurement (Fig.3.4) were mechanically polished at ND-RD plane (thickness) as mentioned above followed by final electro-polishing using 80% Methanol and 20% Perchloric acid as electrolyte.

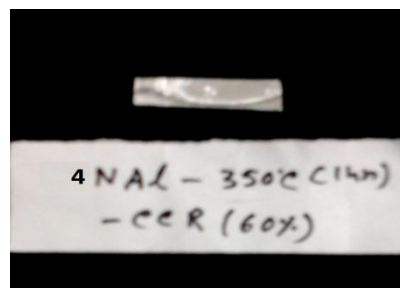


Fig. 3.4: Rolled sheets for EBSD measurement



The bulk texture analysis of the samples was done by using a Panalytical MRD system using Cu- $K_{\alpha}$  radiation (1.54Å). Orthotropic sample symmetry is assumed in each case as the strain imparted in each pass was relatively large ( $\epsilon \geq 0.20$ ). The microstructure and microtexture texture of the deformed materials were characterized by Electron Backscatter Diffraction (EBSD) attached to FEG SEM (FEI, Quanta 3D FEG). EBSD maps were acquired from the ND-RD section of the deformed materials. TSL-OIM<sup>TM</sup> software was used for the analysis of the EBSD data. Bunge notation of Euler angles description is used for representing texture through the ODF.

### **3.3 Hardness Test**

Micro-hardness test was carried out on the RD-ND plane of the deformed samples to characterize and compare their hardness properties. The hardness test was done using a load of 500 g and dwell time of 10 sec. per indentation. Five indentations were taken per sample with a gap of 250 $\mu$ m and the average hardness value was determined. These tests were carried out on micro-hardness testing equipment, Dura Scan (EMCO TEST).

# Chapter 4

## Experimental Results

### 4.1 4N Aluminum (4N-Al):

#### 4.1.1 Microstructure and texture of starting material

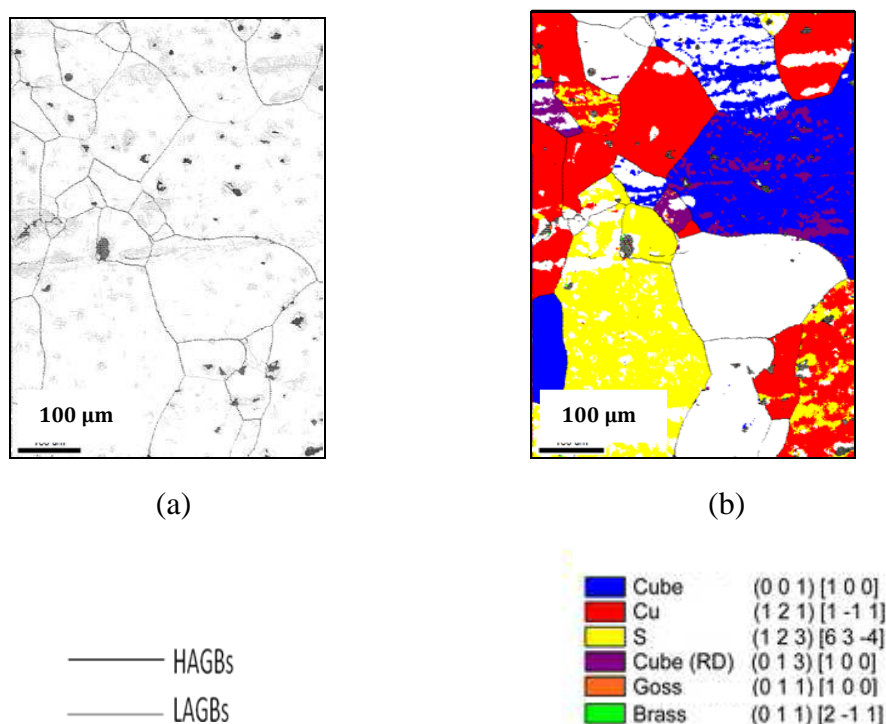


Fig.4.1: (a) GB and (b) orientation maps of as-received 4N-Al

Figure 4.1 (a) shows the GB map (GB map) acquired from the RD-TD section of the 4N-Al as-received material. The HAGBs (misorientation angle  $\theta \geq 15^\circ$ ) are highlighted in black lines in the map while the grey lines represent the LAGBs ( $15^\circ \geq \theta \geq 2^\circ$ ) in the map (this convention is followed in all subsequent maps furnished in this section). Here we can see that starting material is fully recrystallized having sufficiently large starting grain size. Figure 4.1 (b) shows the corresponding orientation map. The typical texture components considered are summarized in

Table 4.1. The quantitative analysis of the microtexture in the starting material shows abundance of C (~18.4%), S and Cu regions.

**Table 4.1: Typical deformation texture components considered in this work**

Orientation	{hkl}<uvw>	( $\phi_1, \phi, \phi_2$ )	Notation	Highlighting color
Cube	{001}<100>	(0,0,0)	C	blue
Rotated cube	{013}<100>	(0,19°,0°)	C <sub>RD</sub>	purple
Copper	{112}<111>	(90°,35°,45°)	Cu	red
S	{123}<634>	(59, 36.7, 63.4)	S	yellow
Brass	{110}<112>	(35.3°, 45°, 0°)	B <sub>S</sub>	green
Goss	{110}<001>	(45°,45°,0°)	G	orange

#### 4.1.2 Deformation by unidirectional cold rolling (UCR)

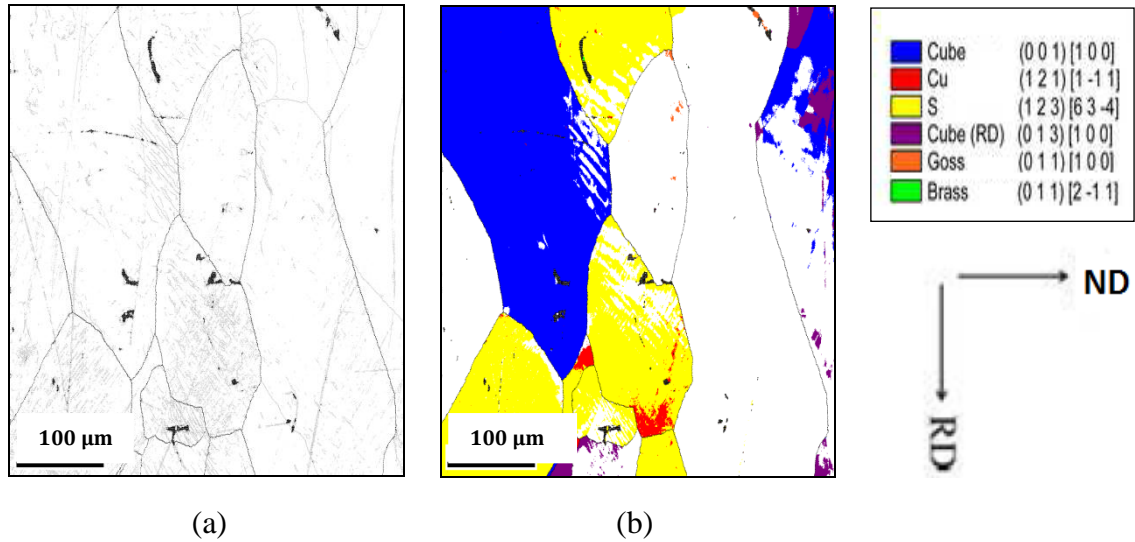


Fig.4.2: (a) GB and (b) orientation maps of 20% deformed UCR processed 4N-Al

Figure 4.2 (a) shows the GB map obtained from the ND-RD section of the UCR processed 20% deformed material. The GB map in this condition resembles the starting recrystallized

microstructure. Inside the deformed grains LAGB network can be easily seen which possibly indicate the development of sub-grain structure. The corresponding orientation map is shown in Fig.4.2 (b). The quantitative analysis of the microtexture from Fig.4.2 (b) shows abundance of C and S oriented regions in the 20% UCR processed material.

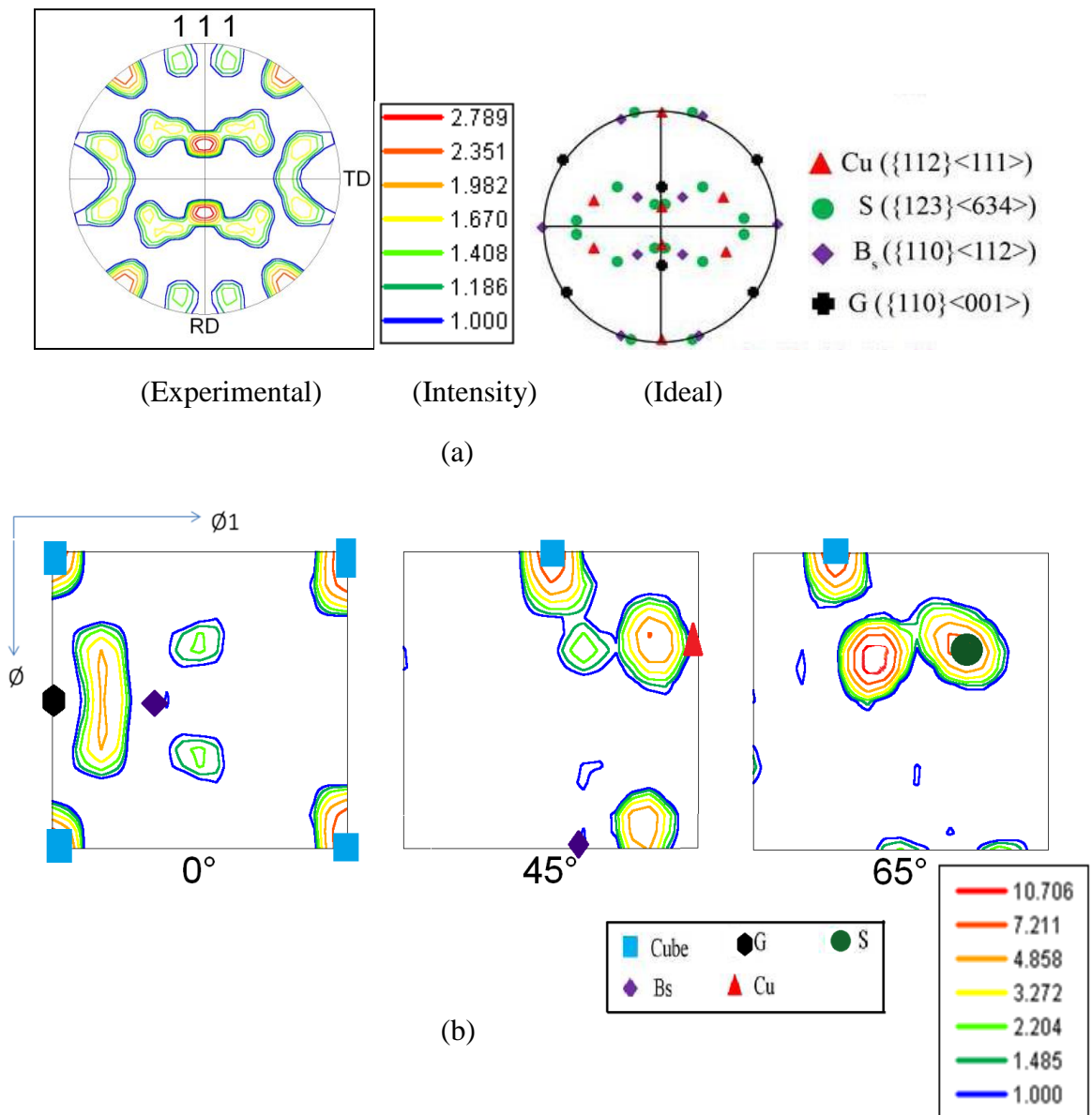


Fig.4.3: (a) (111) PF and (b) ODF of 20% deformed UCR processed 4N-Al

Figure 4.3 (a) shows the (111) PF of UCR processed 20% deformed material. The locations of the typical deformation texture component are shown in an ideal (111) PF in juxtaposition.

Comparison of the (111) PF of processed material with (111) PF showing ideal locations of typical deformation texture components reveals strong presence of the S component and very little amount of the Cu component as strong intensities are found around the ideal S, Cu component. B<sub>S</sub> and Goss component appear rather weak.

The result obtained from (111) PF is amply corroborated from Fig.4.3 (b) which shows the  $\phi_2=0^\circ$ ,  $45^\circ$  and  $65^\circ$  sections of ODF of 20% UCR processed material. From  $\phi_2=65^\circ$  we can see that strong intensities are found around or near to the ideal S locations which indicates the presence of stronger S component. From the ODF presence of the cube(C) component could be observed.

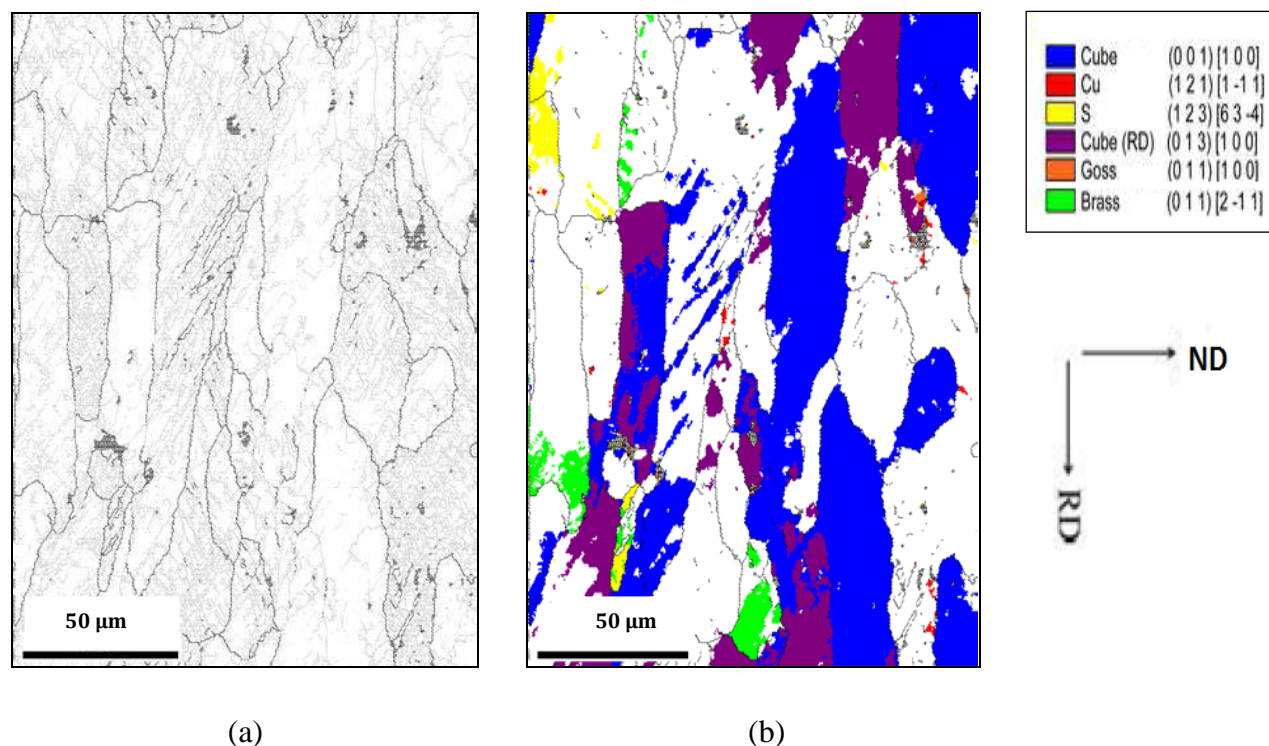
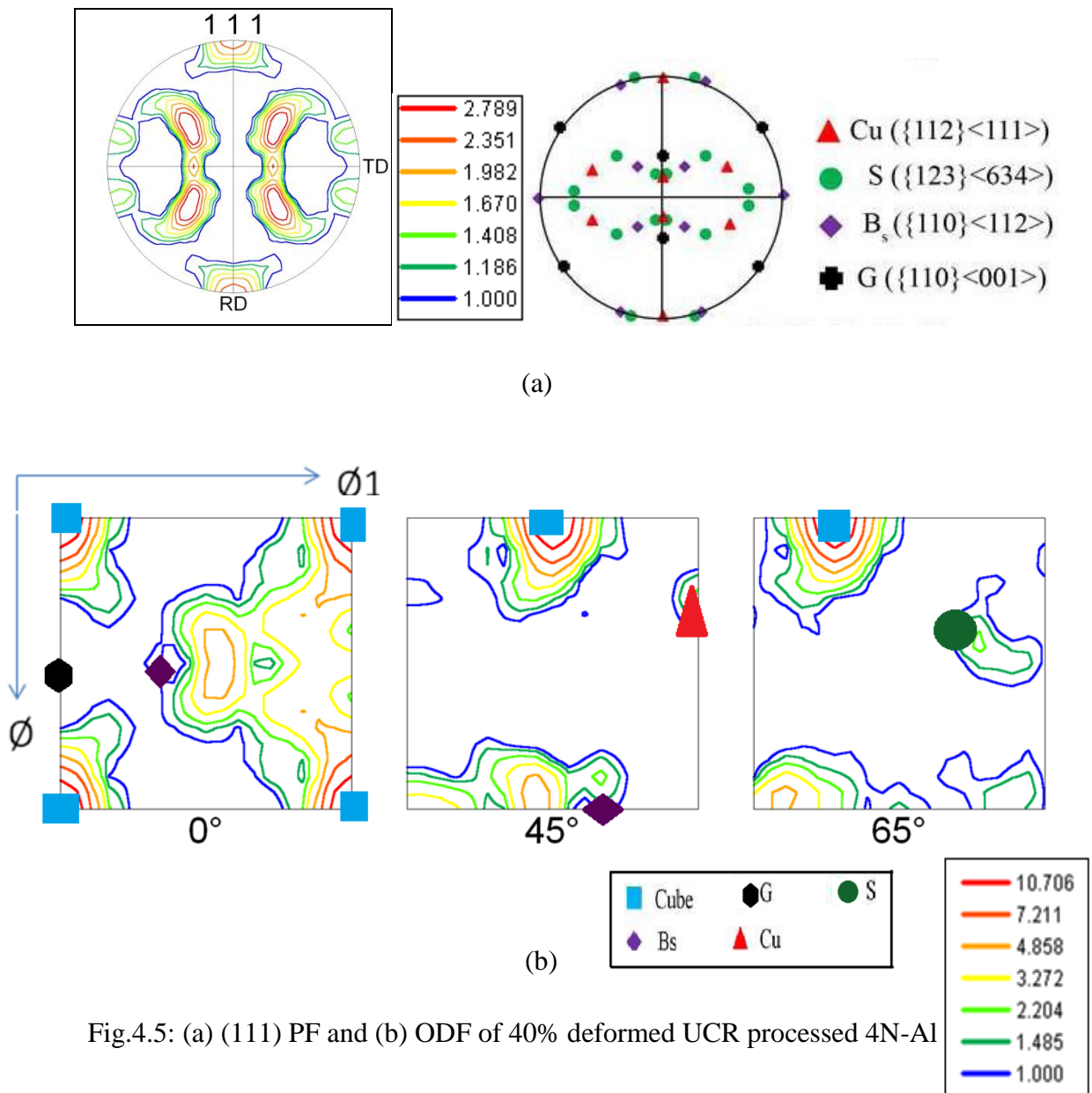


Fig.4.4: (a) GB and (b) orientation maps of 40% deformed UCR processed 4N-Al

Figure 4.4 (a) shows the GB map of the 4N-Al after 40% deformation by UCR route. The microstructure appears elongated along the RD but the development of LAGB network inside the grains is much more prominent in this condition. Figure 4.4 (b) shows the corresponding

orientation map. The quantitative analysis of the microtexture shows remnant C and  $C_{RD}$  oriented regions with almost negligible presence of other texture components. The texture development in this case is also clearly demonstrated by the (111) PF (Fig.4.5 (a)) and the relevant ODF sections (Fig.4.5 (b)). A comparison of the (111) PF of the experimental material with (111) PF showing the ideal locations of typical deformation texture components reveals strong presence of the C component.  $B_s$  and G components are almost absent.



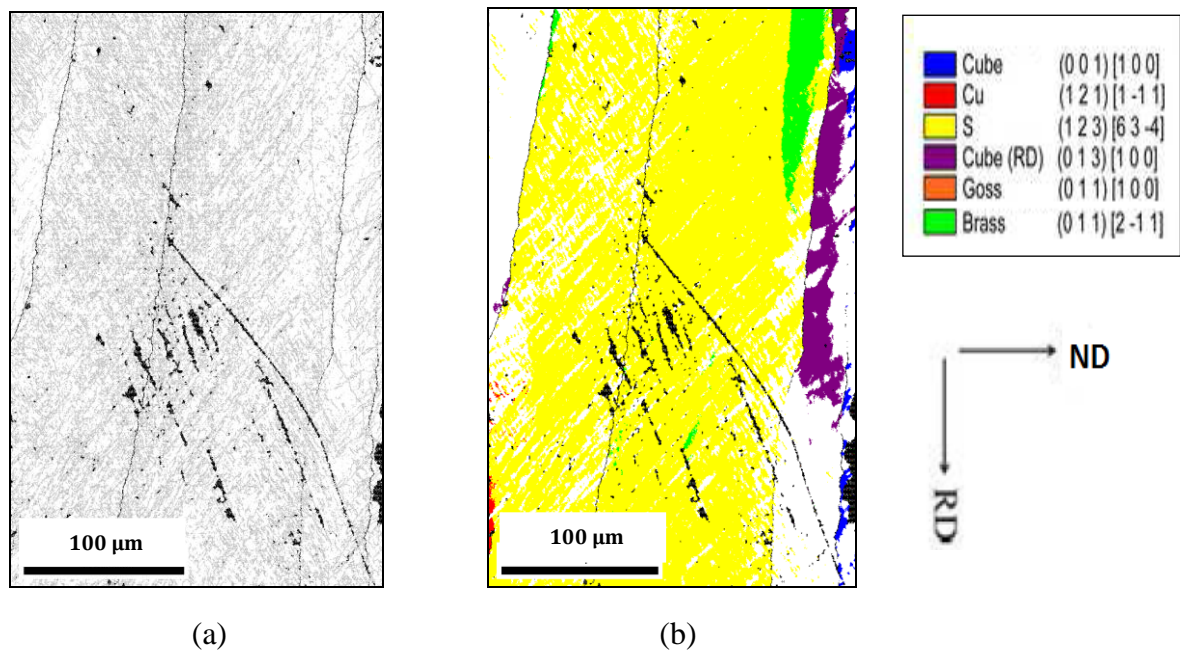


Fig.4.6: (a) GB and (b) Orientation maps of 60% deformed UCR processed 4N-Al

Figure 4.6 (a) shows the GB map of the 60% UCR processed material. An elongated microstructure with extended HAGBs running parallel to the RD evolves after 60% deformation. The structure even after 60% deformation appears to be rather coarse. The quantitative analysis of the microtexture shows presence of profuse S oriented regions which is also supported from the (111) PF (Fig. 4.7(a)) and the relevant ODF sections (Fig.4.7 (b)).

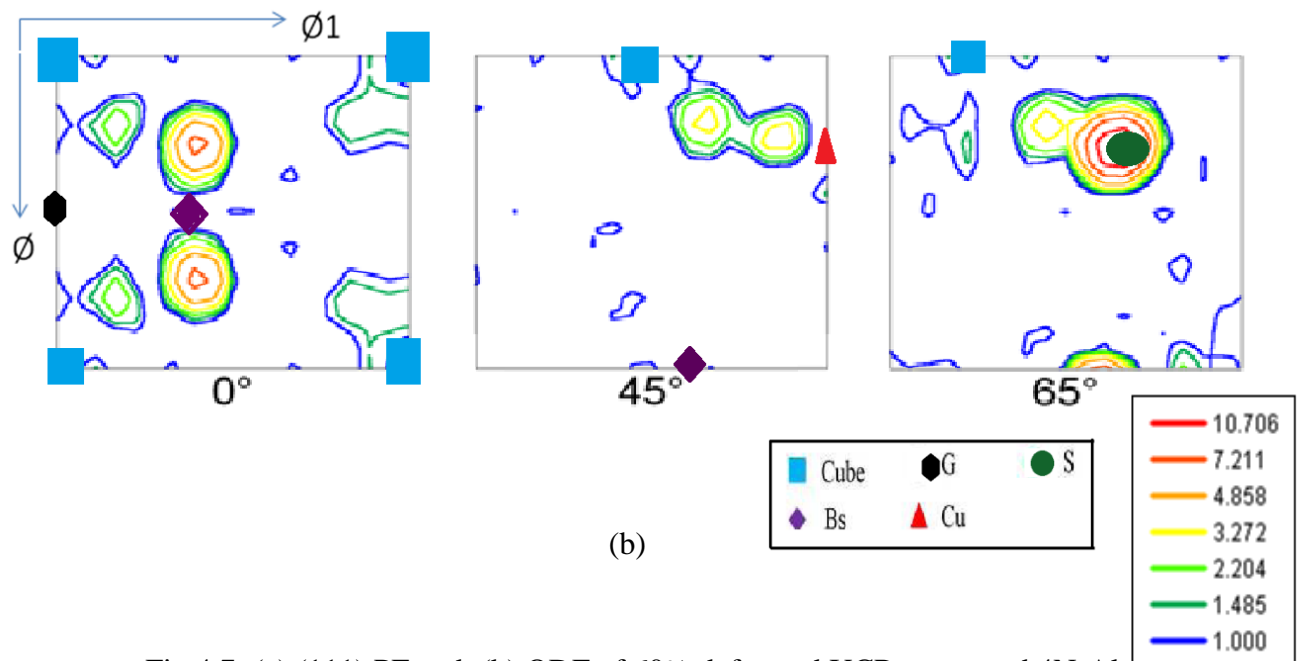
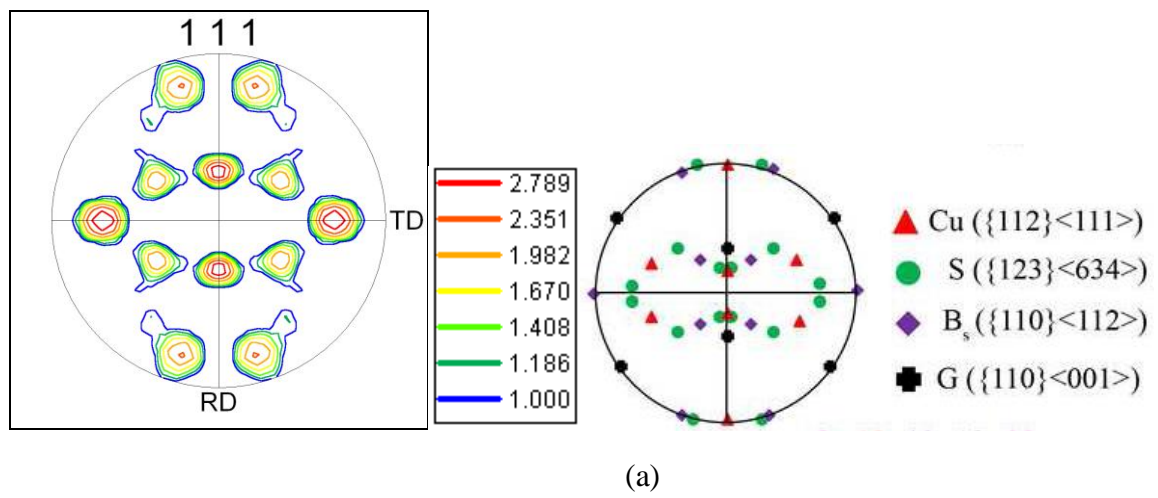


Fig.4.7: (a) (111) PF and; (b) ODF of 60% deformed UCR processed 4N-Al



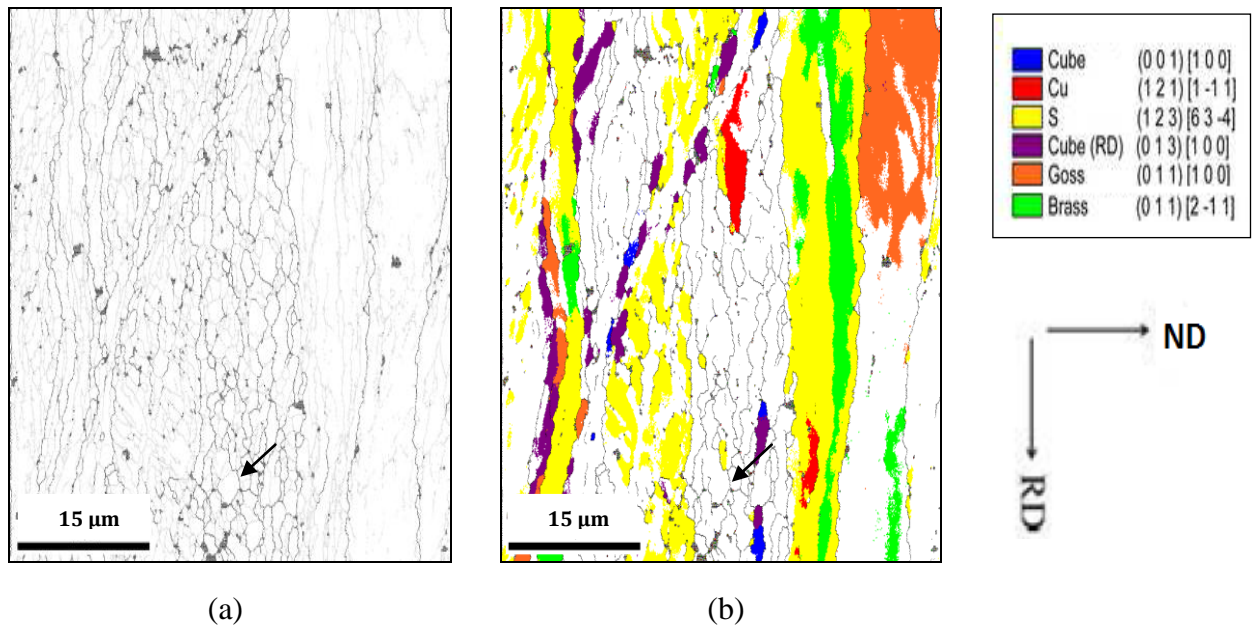
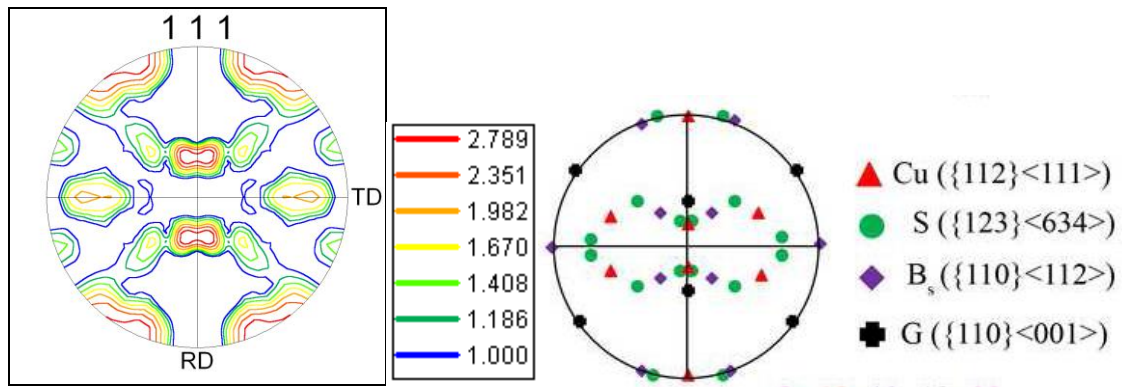
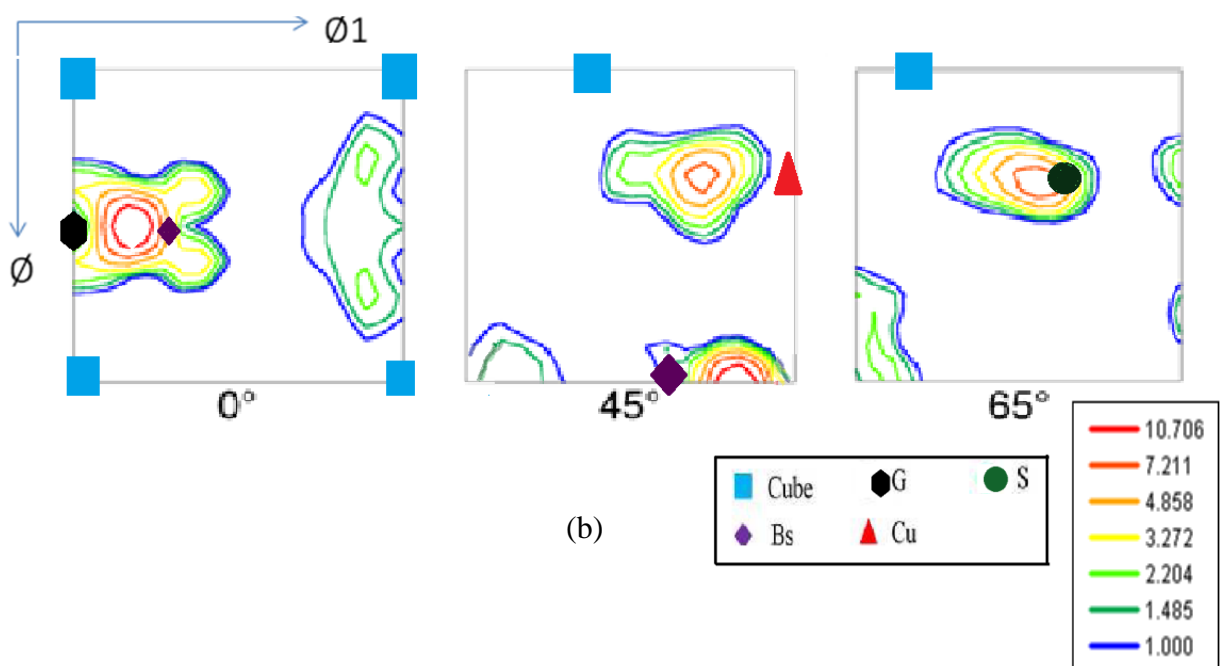


Fig.4.8: (a) GB and (b) orientation maps of 90% deformed UCR processed 4N-Al

Figure 4.8(a) shows the GB map of the 90% UCR processed material. A clear lamellar type structure sub-divided by HAGBs along the ND evolves after 90% deformation although some regions with sub-grains completely engulfed by HAGBs from all sides could also be observed (indicated by the arrow mark in Fig.4.8 (a) and 4.8(b)). However, the HAGB fraction is only about 32% in this condition indicating the presence of relatively large fraction of LAGB (0.68). The corresponding orientation map Fig. 4.8 (b) shows the presence of S oriented regions along with Cu (red), Goss (orange) and  $B_S$  (green) components. These observations are also supported from the (111) PF (Fig.4.9 (a)) and corresponding ODF sections (Fig.4.9 (b)). The  $\phi_2 = 45^\circ$  section of the ODF indicates that  $B_S$  and Cu components are shifted from their respective ideal locations along the  $\phi_1$  axis.



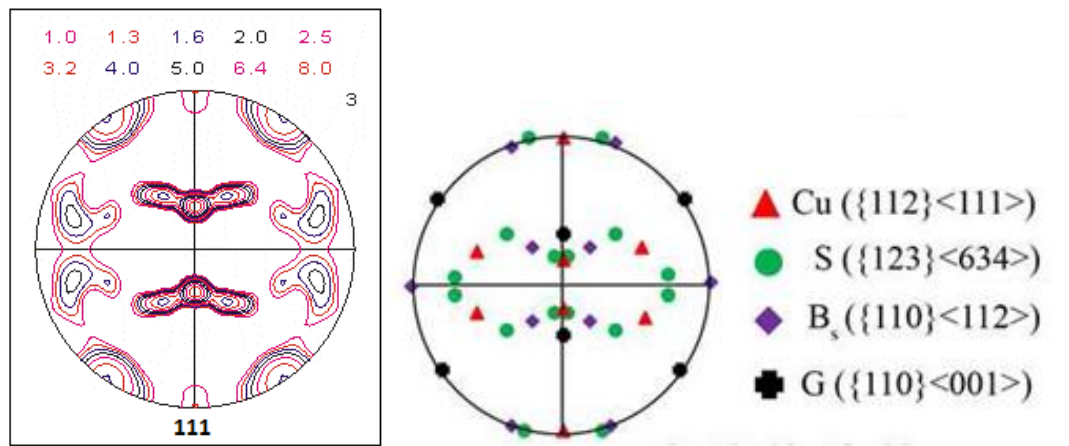
(a)



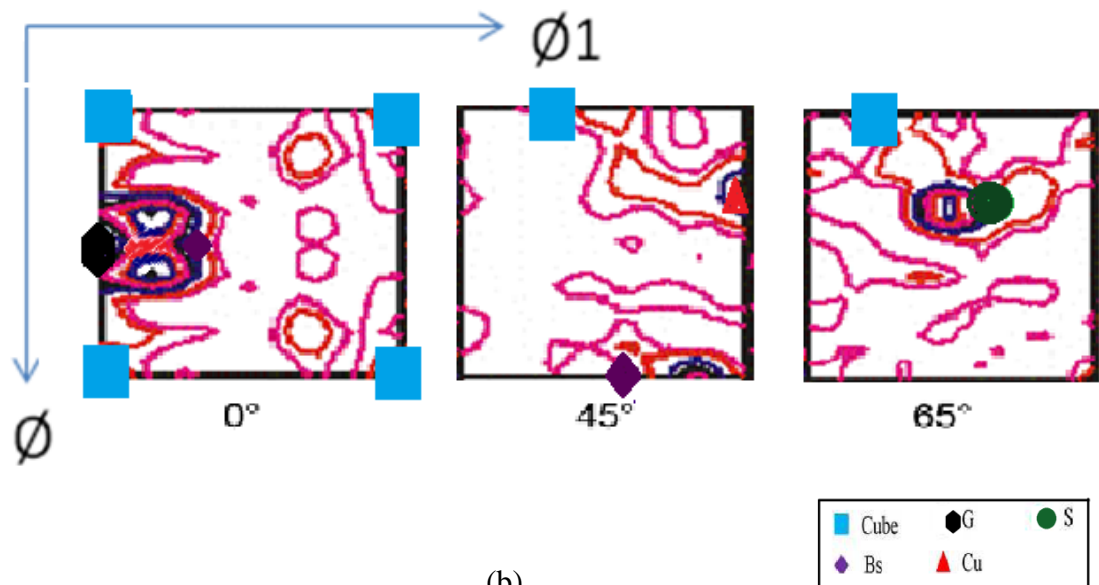
(b)

Fig.4.9: (a) (111) PF and (b) ODF of 90% deformed UCR processed 4N-Al

The bulk texture of the 90% UCR processed material is further analysed by XRD. The (111) PF and the full ODF are shown in Fig.4.10 (a) and 4.10(b), respectively. The (111) PF clearly indicate the presence of  $B_s$ , S and Cu orientation. Here also the  $B_s$  component appears somewhat shifted from the ideal location along the  $\phi_1$  axis indicating the existence of ND-rotated  $B_s$  orientation ( $B_s^{ND}$ ).



(a)



(b)

Fig.4.10: (a) (111) PF and (b) ODF of 90% deformed UCR processed 4N-Al measured by XRD

### 4.1.3 Deformation by cross cold rolling (CCR)

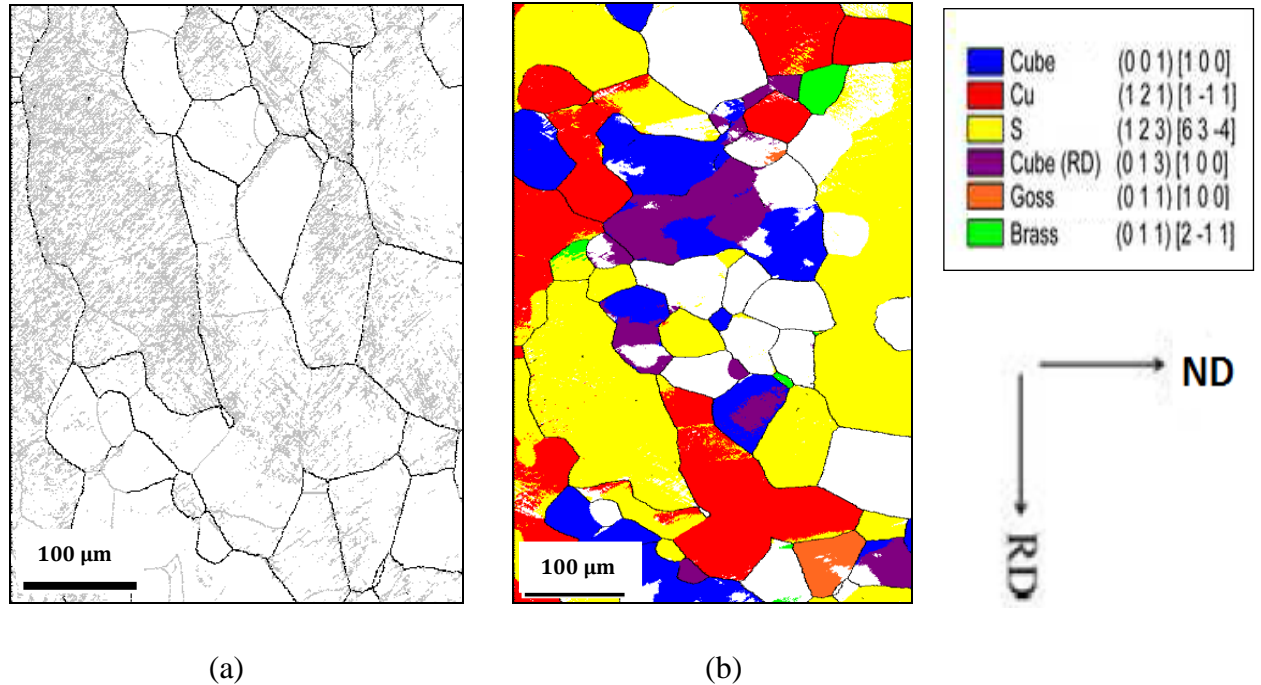


Fig.4.11: (a) GB and (b) orientation maps of 20% deformed CCR processed 4N-Al

Figure 4.11(a) shows the GB map acquired from the RD-TD section of the 4N-Al deformed to 20 % reduction in thickness by the CCR route. The microstructure after 20% deformation resembles the starting recrystallized microstructure except for the development of LAGB network inside the grains. Fig. 4.11(b) is the corresponding orientation map showing the presence of profuse S and Cu oriented regions.  $C_{RD}$  (purple) and C (blue) components also exist in sufficient amount. Goss (orange) and Bs (green) components, however, appear to be rather weak. The distribution of microtexture components in this deformed condition is also amply corroborated by the corresponding (111) PF (Fig.4.12 (a)) and ODF section (Fig.4.12 (b)).

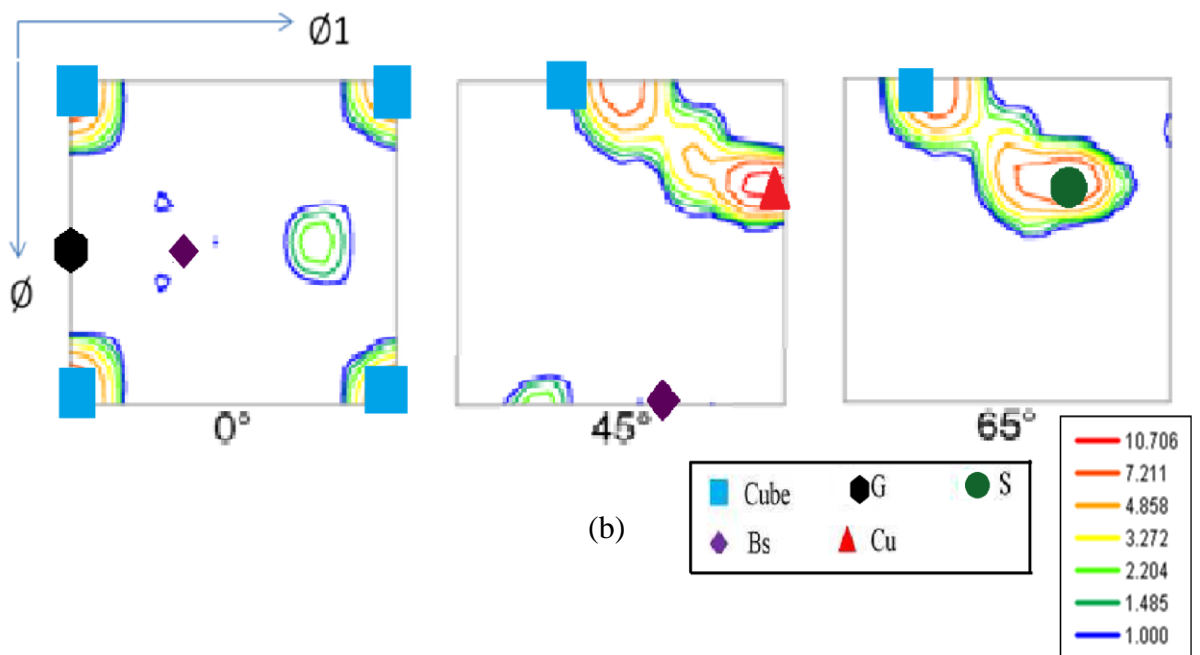
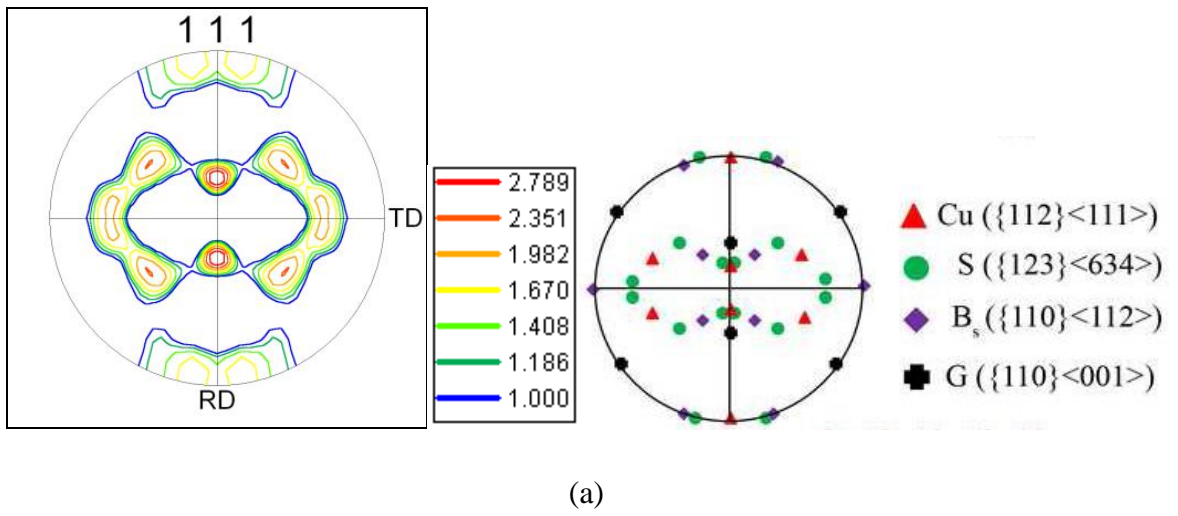


Fig.4.12: (a) (111) PF and (b) ODF of 20% deformed CCR processed 4N-Al

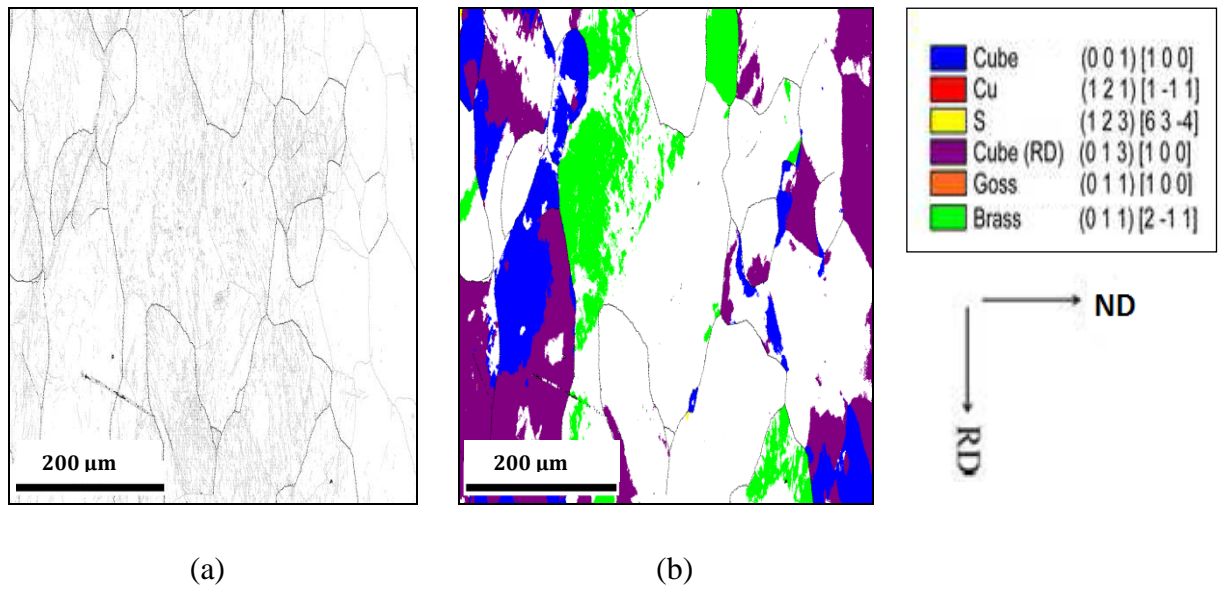
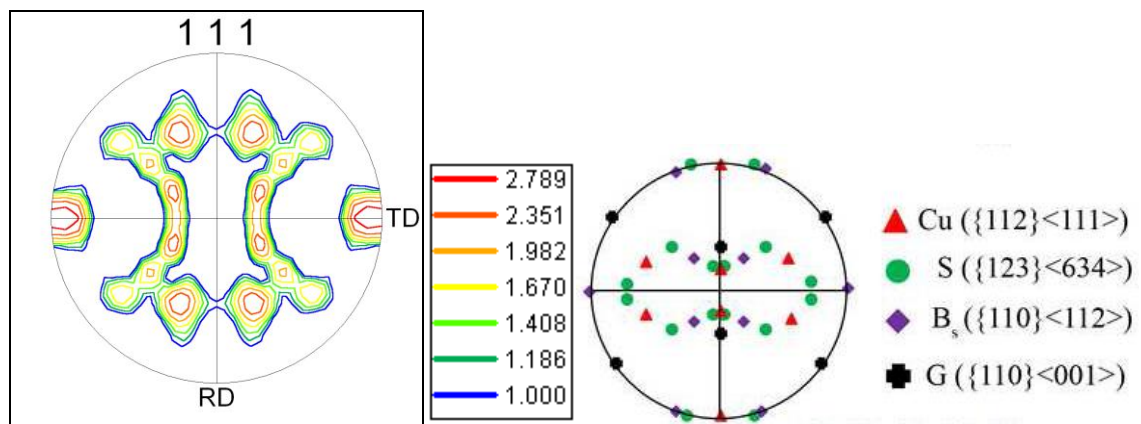
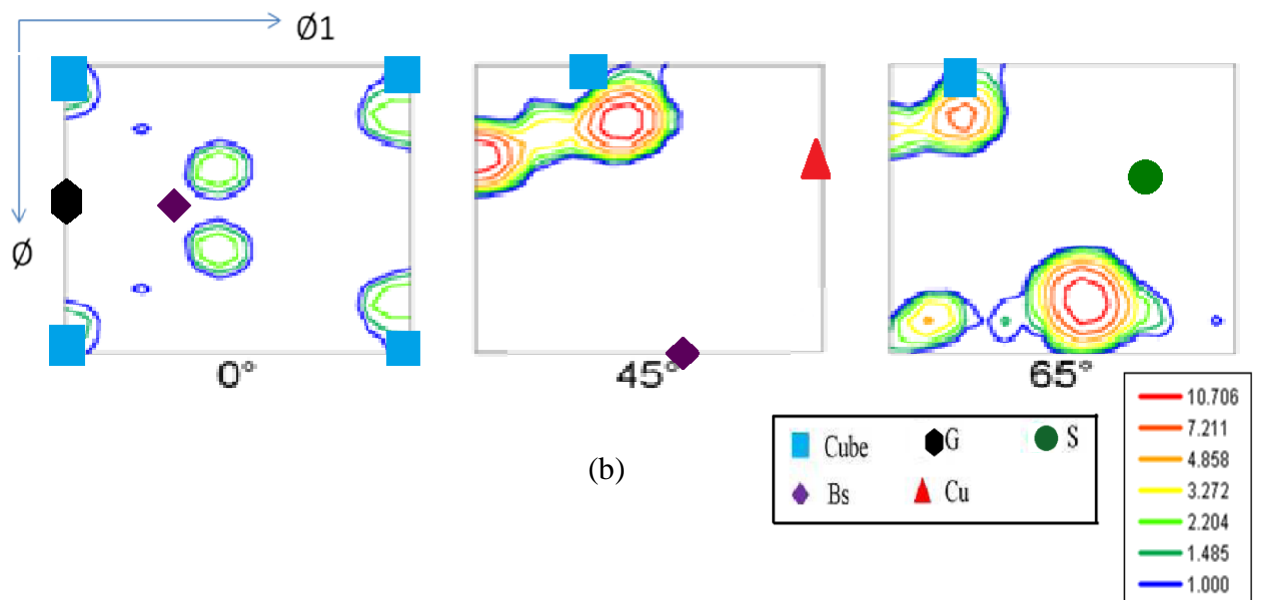


Fig.4.13: (a) GB and (b) orientation maps of 40% deformed CCR processed 4N-Al

Figure 4.13(a) shows the GB map of the 40 % deformed CCR processed material. Few of the grains appear slightly elongated in the direction of the RD while few more equi-axed grains could also be observed. LAGB network inside the grains could be easily observed. Fig. 4.13(b) shows the corresponding orientation map which shows the presence of C,  $C_{RD}$  and  $B_S$  oriented regions in this deformed condition. The relative weaker texture is also evident from the appearance of the (111) PF (Fig.4.14 (a)) and the relevant ODF sections (Fig.4.14 (b)).



(a)



(b)

Fig.4.14: (a) (111) PF (b) ODF of 40% deformed CCR processed 4N-Al

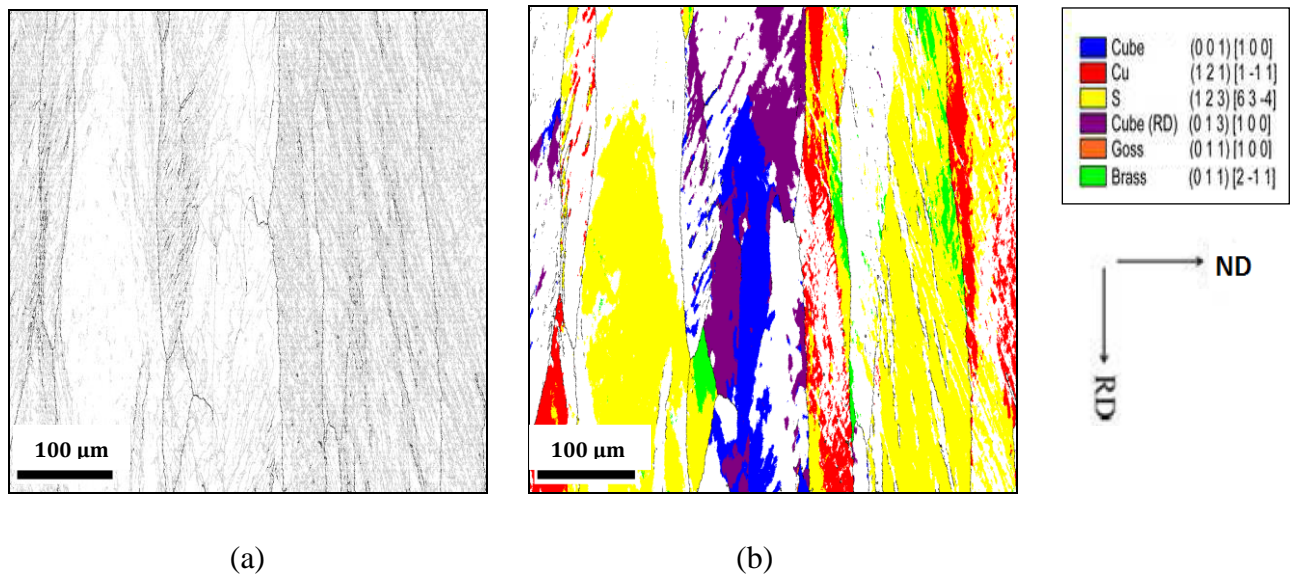
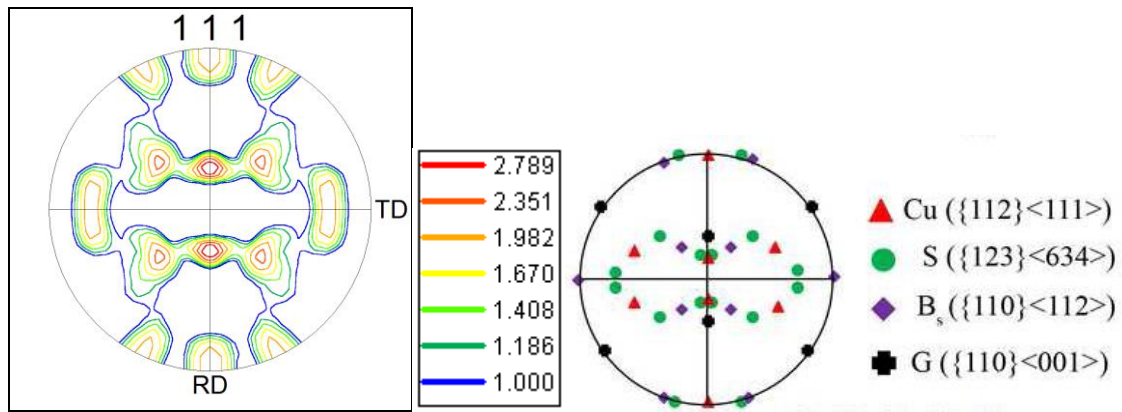


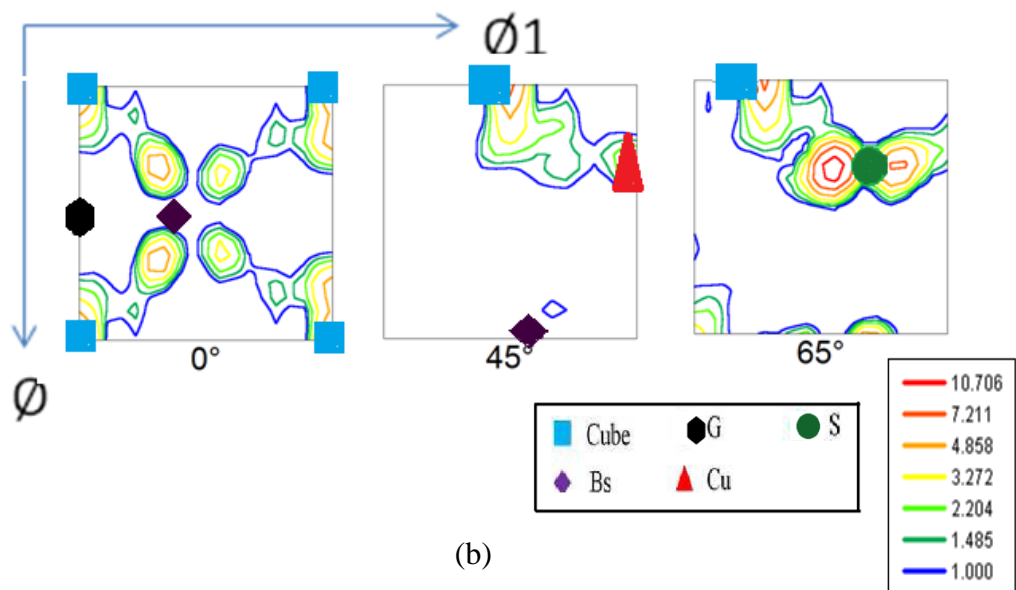
Fig.4.15: (a) GB and (b) orientation maps of 60% deformed CCR processed 4N-Al

Fig.4.15 (a) shows the GB map acquired from 60% deformed material. From OIM analysis of GB map we find that the fraction of LAGBs (0.825) is more than the fractions of HAGBs (0.175). The microstructure still appears quite coarse at this stage. Fig.4.15 (b) shows the orientation map acquired from the same place as explained above. The HAGBs (misorientation angle  $\theta \geq 15^\circ$ ) are highlighted in black lines in the map. The quantitative analysis of the microtexture ( $15^\circ$  cut-off angle is used for calculating the volume fractions) shows abundance of S and Cu oriented regions in the 60% deformed CCR processed 4N-Al.





(a)



(b)

Fig.4.16: (a) (111) PF and (b) ODF 60% deformed CCR processed 4N-Al

Figure 4.16 (a) shows the (111) PF of 60% deformed CCR processed 4N-Al. Comparison of the (111) PF of processed material with (111) PF showing ideal locations of typical deformation texture components reveals strong presence of the S( $\{123\}\langle 63-4\rangle$ ) and Cu( $\{112\}\langle 1-11\rangle$ ) components. The result obtained from (111) PF is amply corroborated Fig.4.16 (b) which shows the  $\phi_2=0^\circ$ ,  $45^\circ$  and  $65^\circ$  sections of ODF of 60% CCR processed 4N-Al.

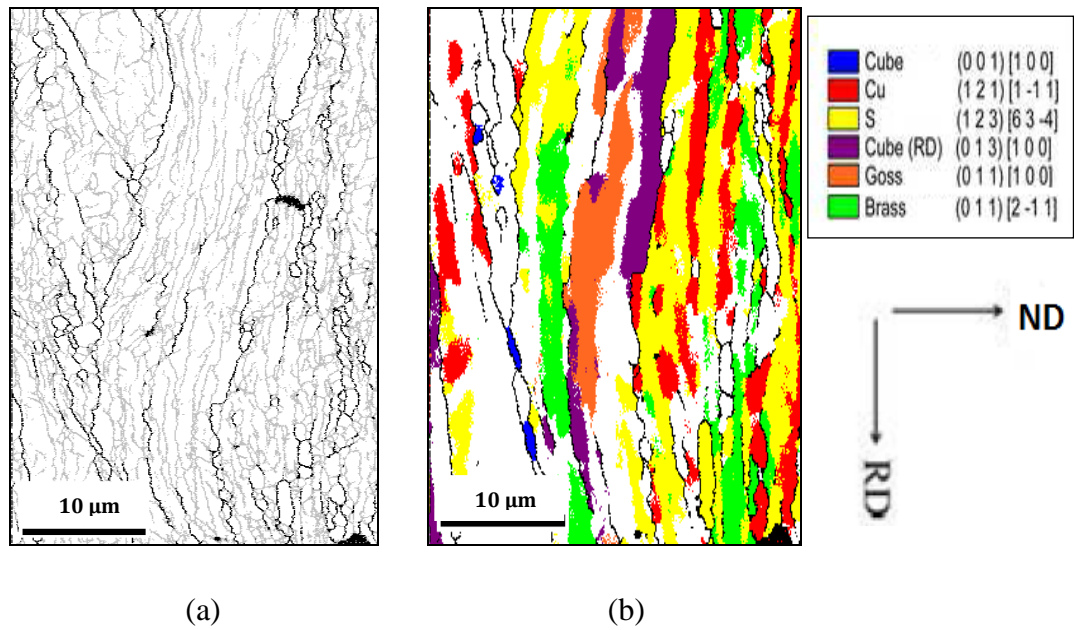
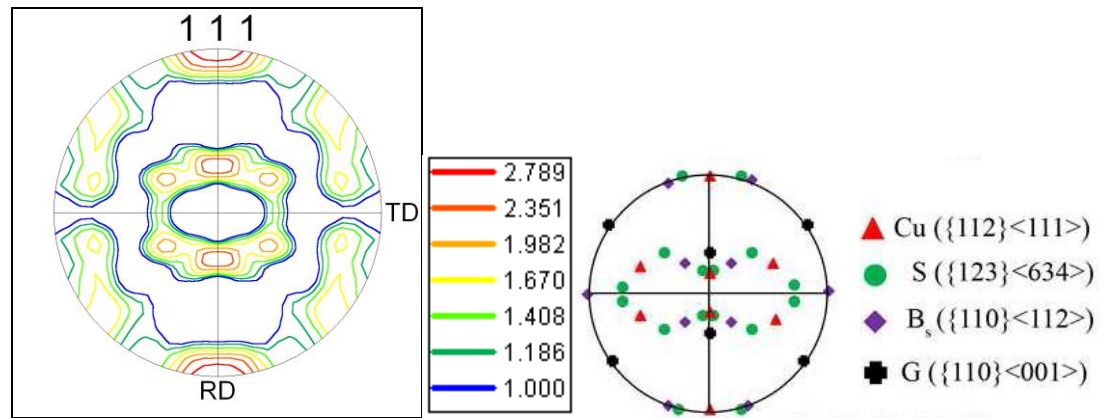
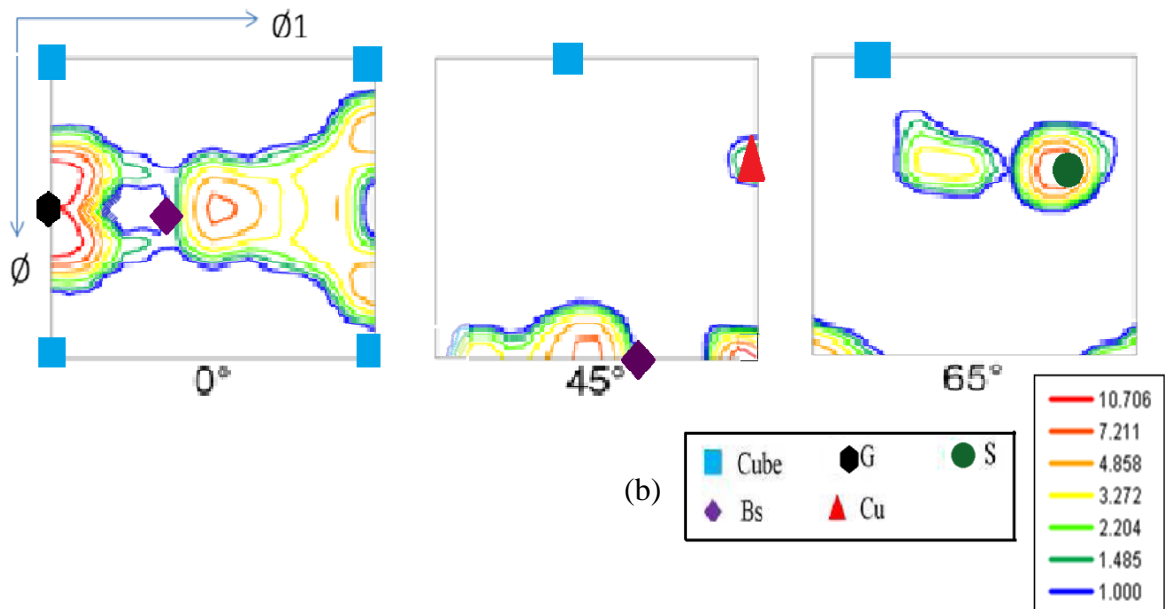


Fig.4.17: (a) GB and (b) orientation maps of 90% deformed CCR processed 4N-Al

Figure 4.17(a) shows the GB map following 90% deformation by the CCR route. The wavy appearance of the microstructure is probably due to the effect of local shearing. The fraction of HAGBs in this condition is found to be 0.20. Figure 4.17(b) shows the corresponding orientation map which reveals the presence of the typical deformation texture components such as S, Cu and Bs.  $C_{RD}$  and Goss (orange) components are also found. C (blue) component is found to be rather insignificant.



(a)



(b)

Fig.4.18: (a) (111) PF; (b) ODF of 90% deformed CCR processed 4N-Al

Figure 4.18 (a) shows the (111) PF of 90% deformed material processed by the CCR route. Analysis of the PF and the ODF sections reveals presence of the Goss and  $B_s$  (shifted) and S components. The shift of the  $B_s$  component along the  $\phi_1$  axis indicates the presence of  $B_s^{ND}$  orientation.

The texture of the 90% UCR processed material is further analysed by XRD. The (111) PF and the full ODF is shown in Fig.4.19 (a) and 4.19 (b), respectively. The shift of the  $B_s$  component is amply corroborated from the  $\varphi_2=0^\circ$  ODF section.

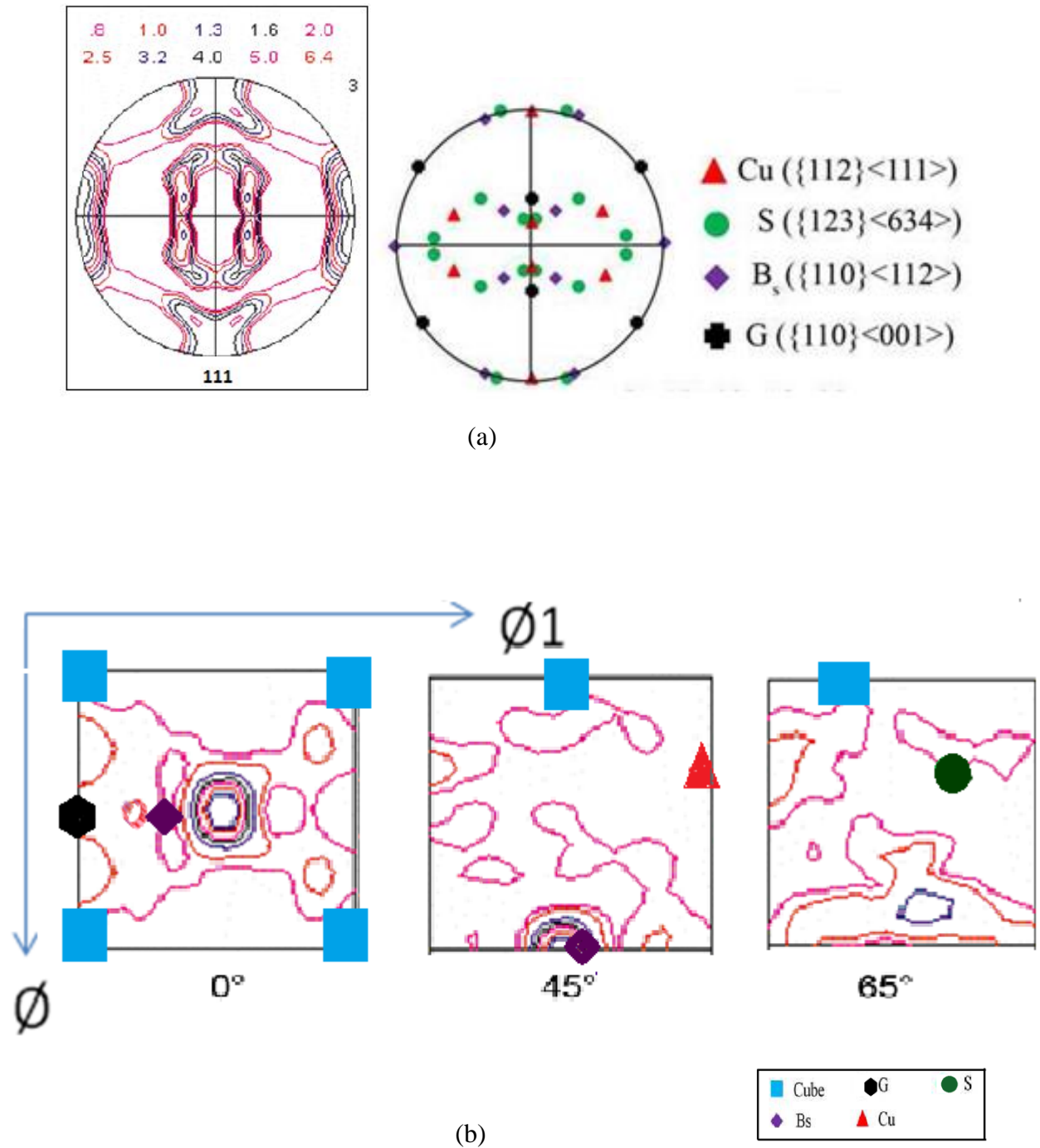


Fig.4.19: (a) (111) PF and (b) ODF of 90% deformed CCR processed 4N-Al measured by XRD

#### 4.1.4 Evolution of Hardness Properties

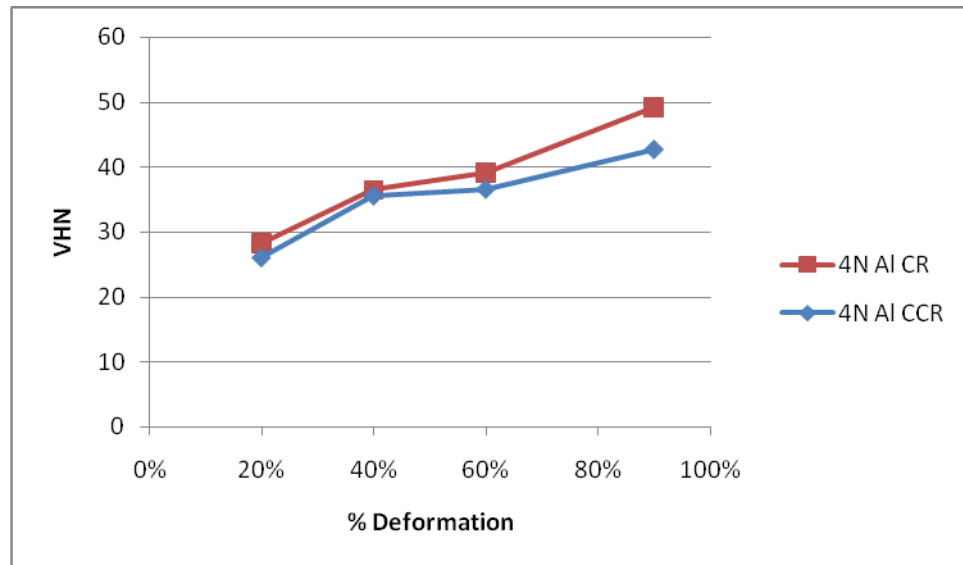


Fig.4.20: Evolution of hardness properties in UCR and CCR processed 4N-Al

Hardness has been measured at the RD-ND plane along the RD. From Fig.4.20 it may be seen that hardness increases with increasing strain for both UCR and CCR processed materials. For 20%, 40% & 60% deformation the hardness values of UCR and CCR processed materials are quite comparable but in case of 90% deformation we can observe a significant difference in the hardness values. UCR processed material clearly shows greater hardness value than its CCR processed counterpart.

## 4.2 Al -2.5% Mg alloy

### 4.2.1 Microstructure and texture of starting material

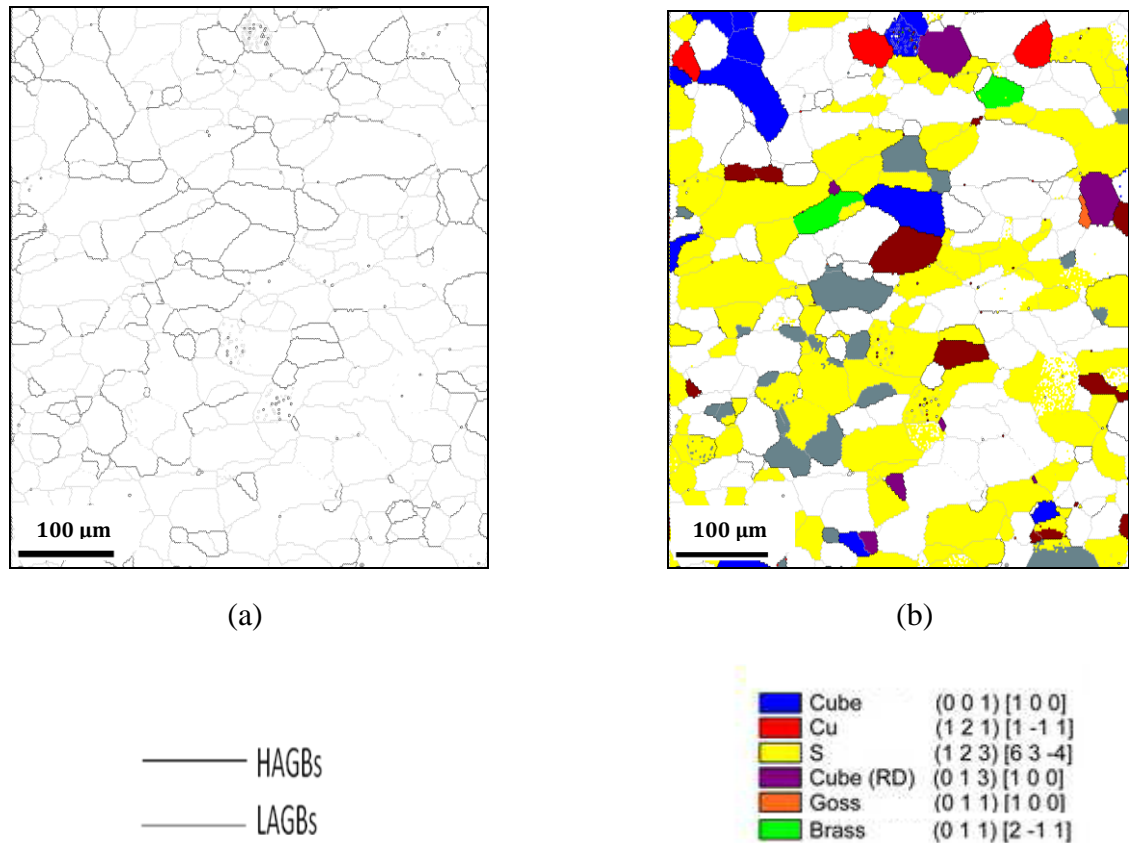


Fig.4.21: (a) GB and (b) orientation maps of as-received Al-2.5% Mg alloy

Figure 4.21(a) shows the GB map acquired from the RD-TD section of the starting Al-2.5%Mg alloy. The starting material is fully recrystallized with an average grain size of 27μm. Figure 4.21(b) shows the corresponding orientation map. The quantitative analysis of the microtexture shows strong S component in the starting material.

## 4.2.2 Deformation by unidirectional cold rolling (UCR)

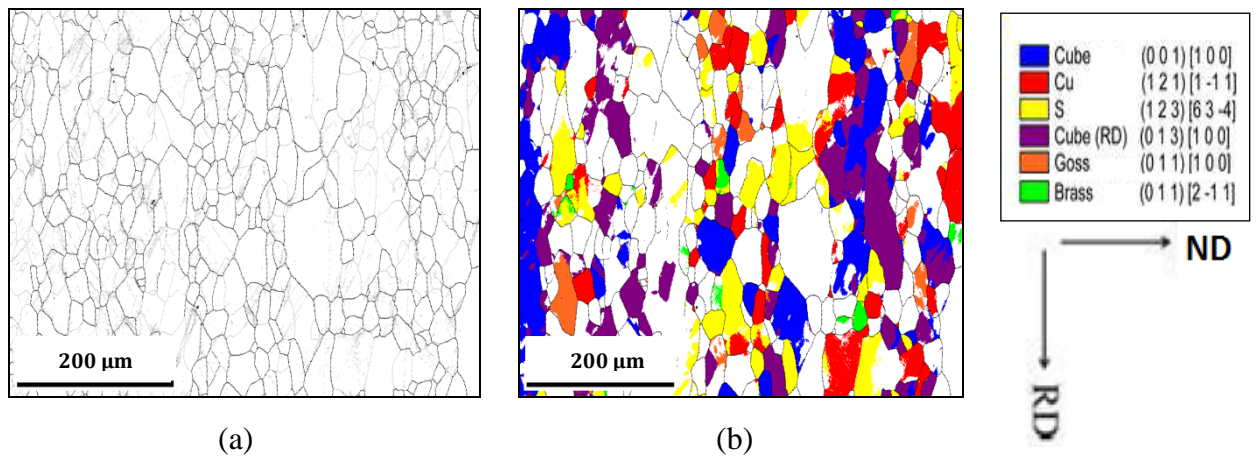
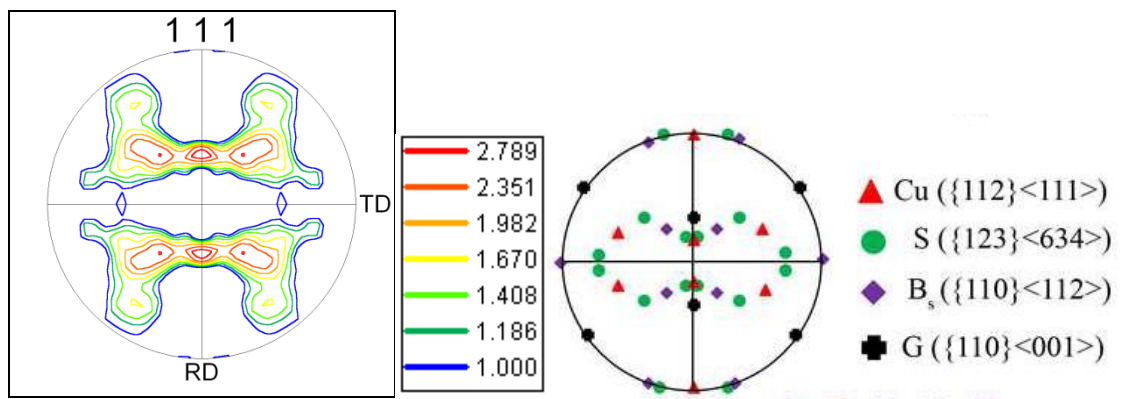
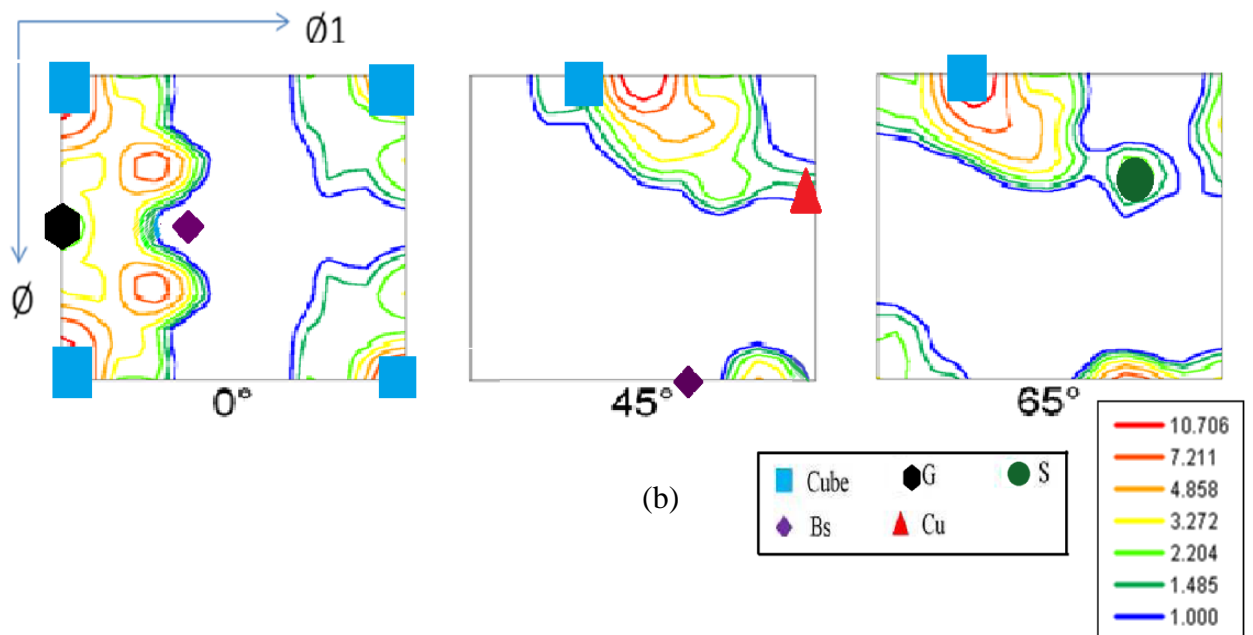


Fig.4.22: (a) GB and (b) orientation maps of UCR processed 20% deformed Al-2.5% Mg Alloy

Figure 4.22(a) shows the GB map of the UCR processed 20% deformed material. The microstructure in this condition appears somewhat similar to the starting recrystallized microstructure. Figure 4.22(b) shows the corresponding orientation map. The quantitative analysis of the microtexture shows profuse C and S oriented regions in this deformed condition. Cu and  $C_{RD}$  components are also observed.



(a)



(b)

Fig.4.23: (a) (111) PF and (b) ODF of UCR processed 20% deformed Al-2.5%Mg alloy

Figure 4.23(a) shows the (111) PF of UCR processed 20% deformed Al-2.5%Mg alloy. The appearance of the PF and ODF (Fig.4.23 (b)) clearly show that the texture is not so well developed in this condition possibly due to the low strain value.



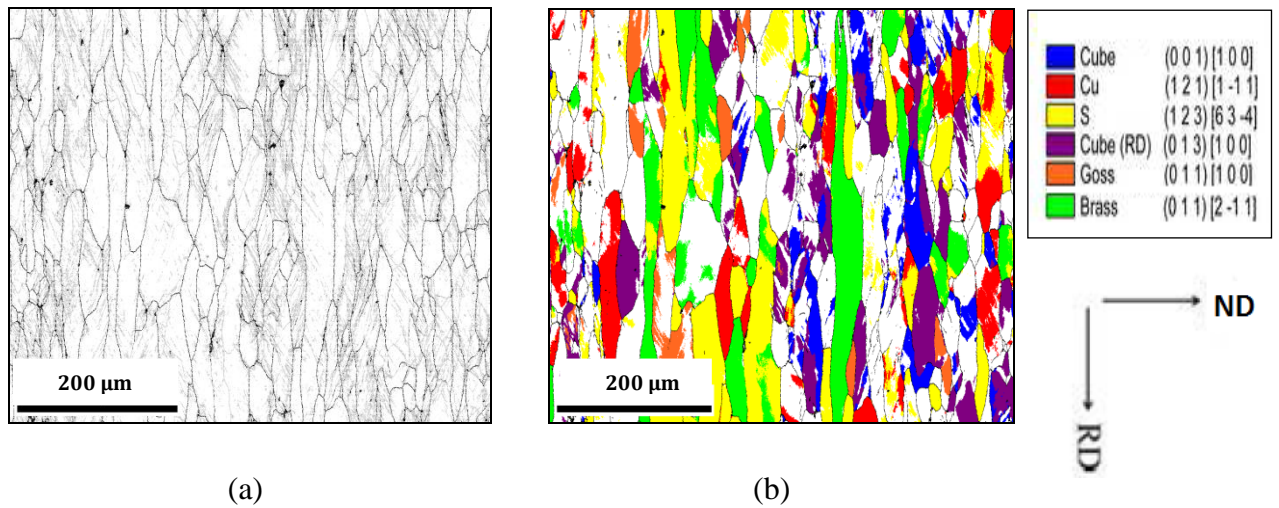
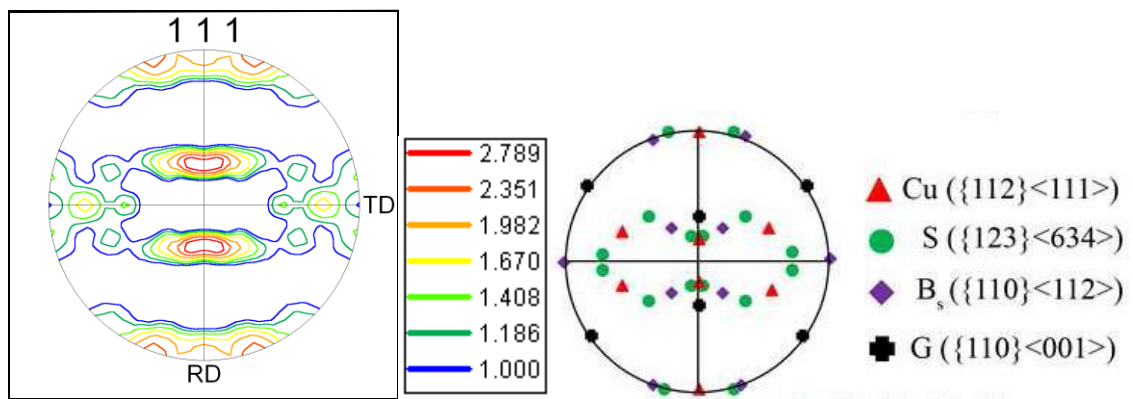
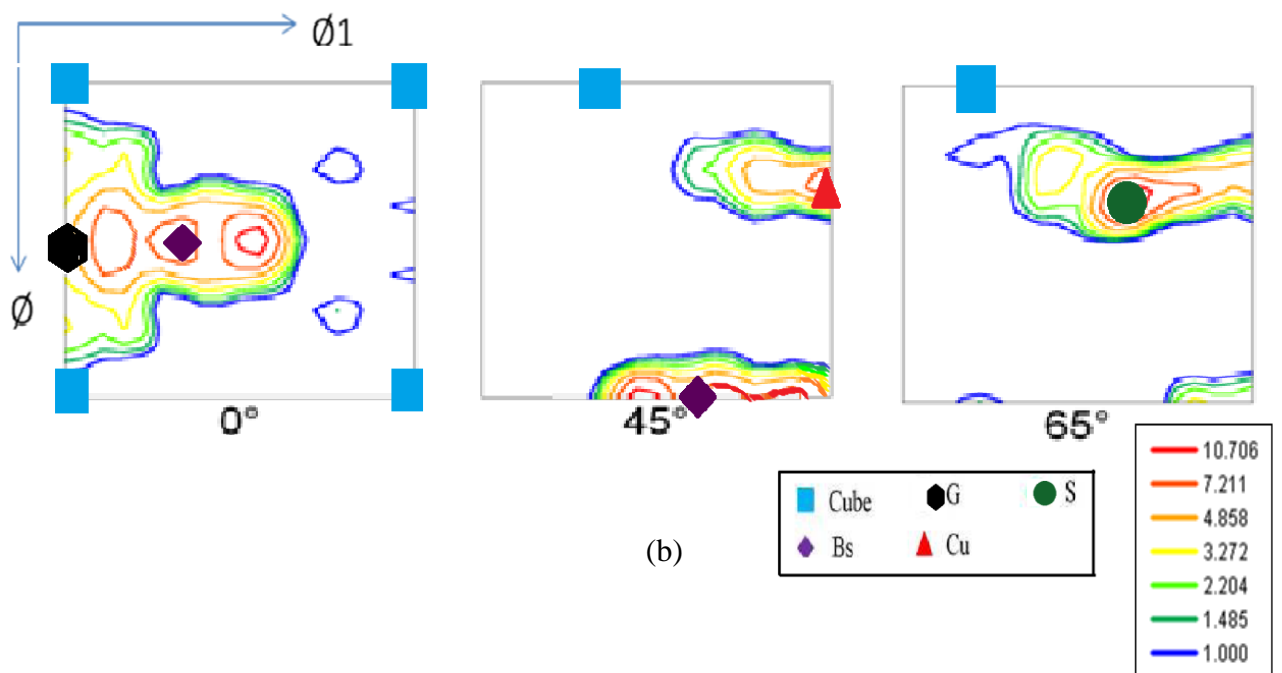


Fig.4.24: (a) GB (b) orientation maps of UCR processed 40% deformed Al-2.5%Mg alloy

After 40% deformation microstructure somewhat elongated along the RD could be easily observed in the GB map (Fig.4.24 (a)). The orientation map (Fig.4.24 (b)) indicates the presence of S, Cu and  $B_S$  as the main deformation texture components. Small fragmented C oriented regions could also be observed. These observations are also amply justified from the appearance of the (111) PF and respective ODF sections Fig.4.25 ((a)-(b)) which indicates the development of typical pure metal or copper type rolling texture.



(a)



(b)

Fig.4.25: (a) (111) PF and (b) ODF of 40% deformed UCR processed Al-2.5%Mg alloy.

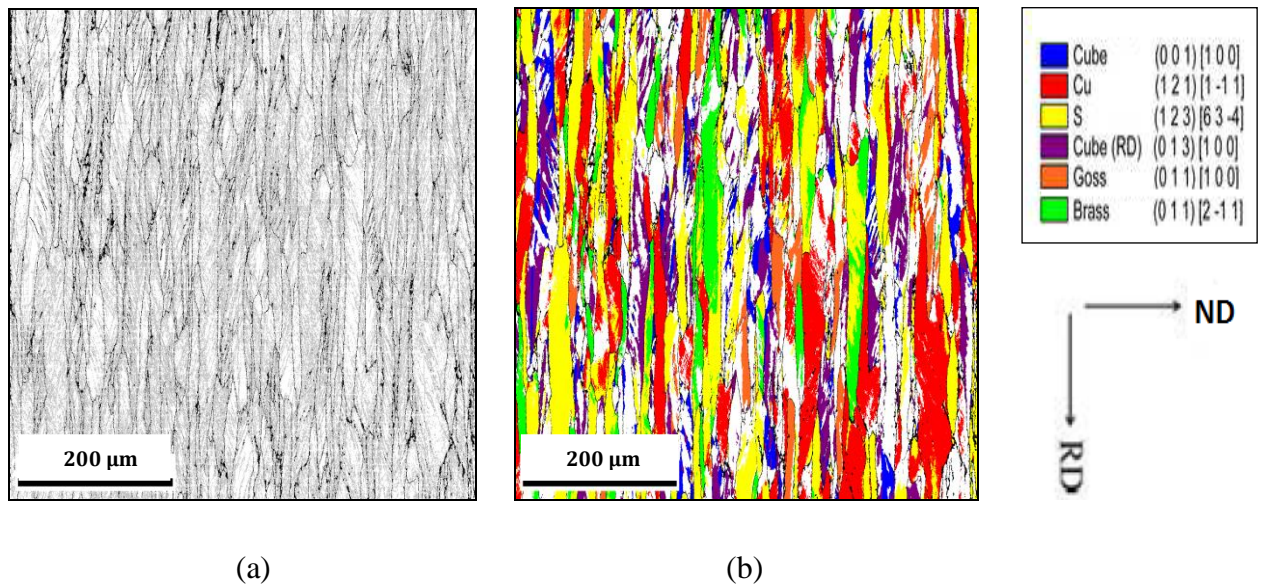
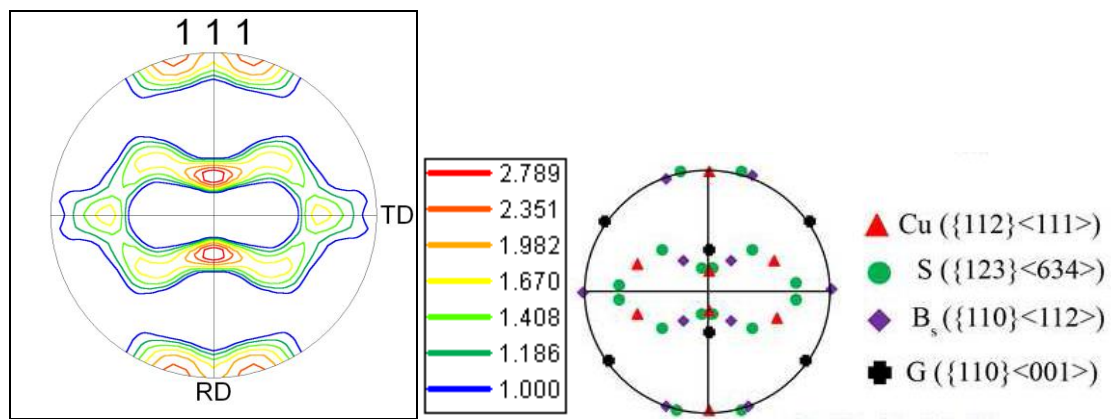


Fig.4.26: (a) GB and (b) orientation maps of UCR processed 60% deformed Al-2.5%Mg alloy

Figure 4.26(a) shows the microstructure of UCR processed Al-2.5%Mg alloy after 60% deformation. The microstructure in this condition is essentially a lamellar structure. Figure 4.26(b) shows the corresponding orientation map. The orientation map indicates the presence of mainly Cu, S & B<sub>s</sub> oriented regions. Other deformation texture components appear to be rather weak. The (111) PF and ODF sections shown in Fig.4.27(a) and 4.27(b) clearly indicate very well developed pure metal or copper type texture in this deformed condition.



(a)

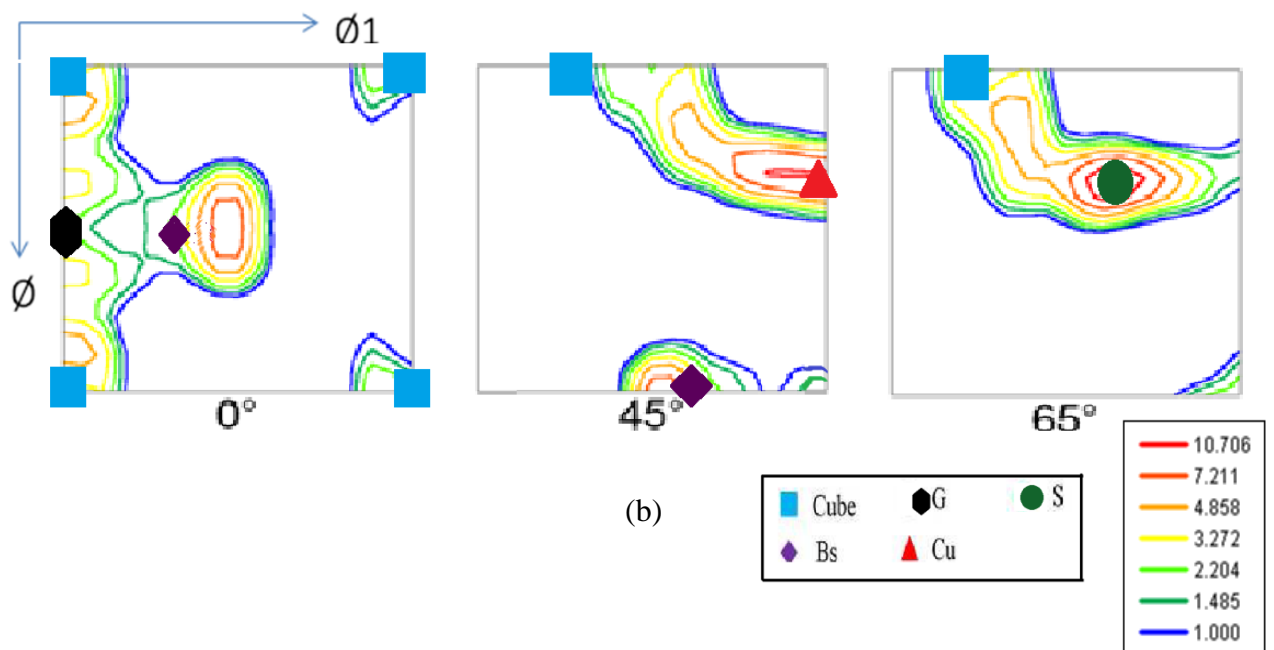


Fig.4.27: (a) (111) PF and (b) ODF of 60% deformed CCR processed Al-2.5%Mg alloy

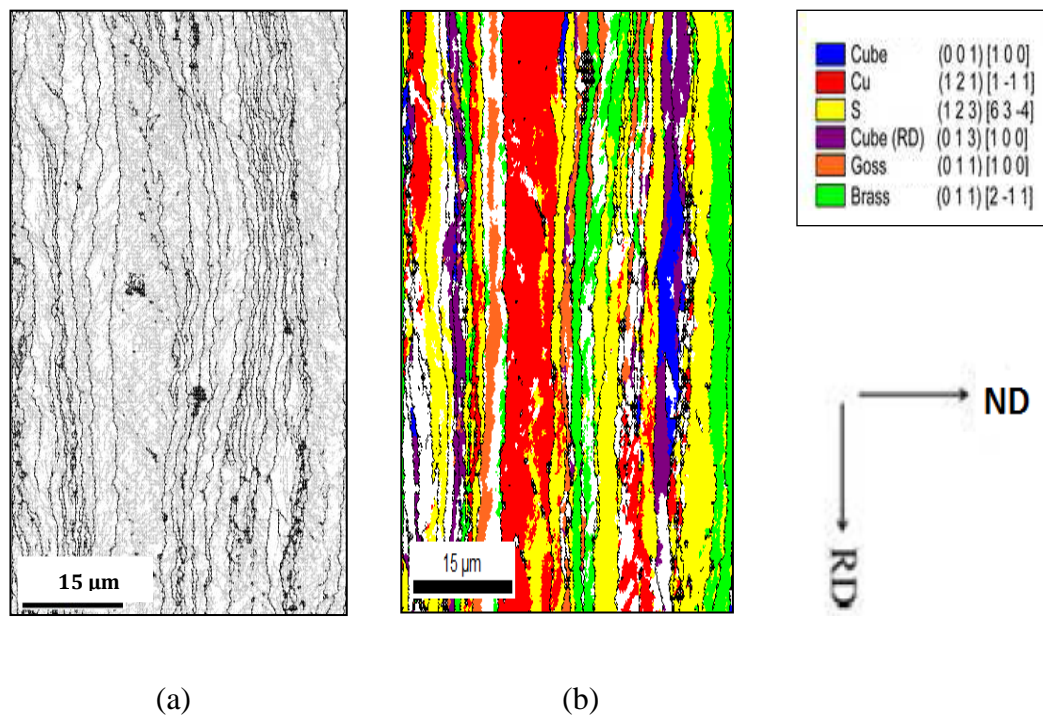
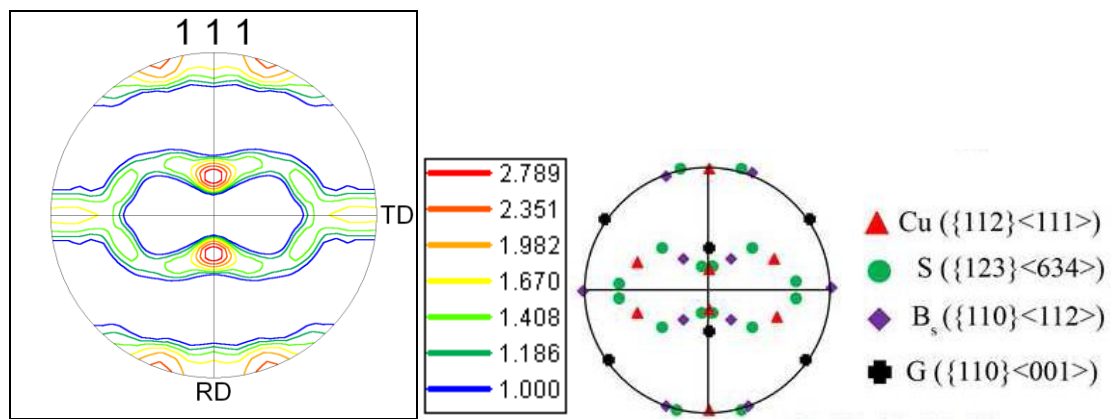
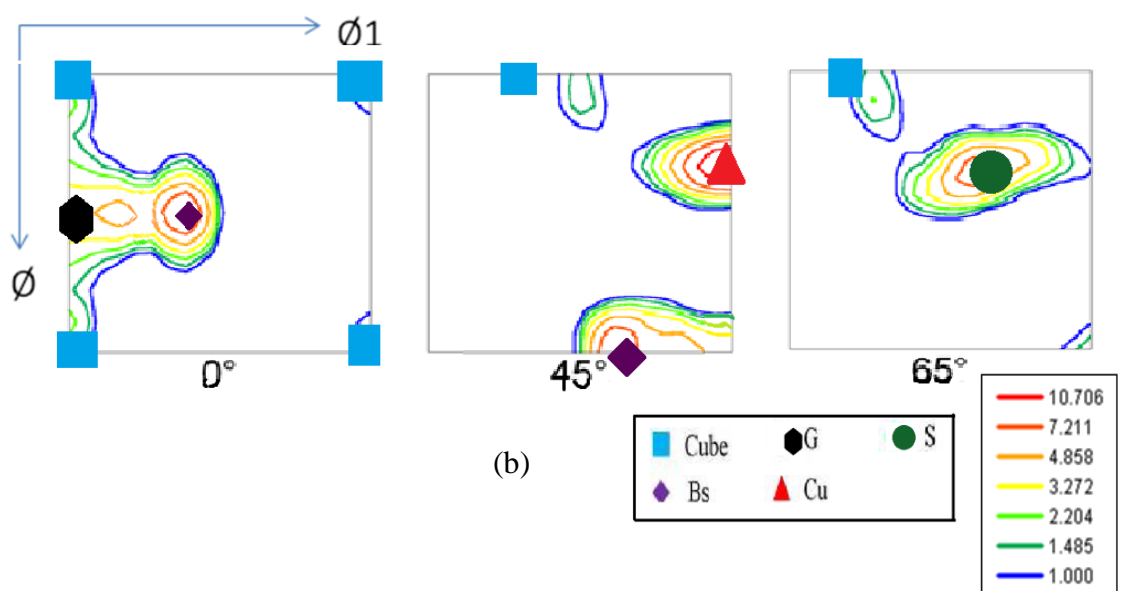


Fig.4.28: (a) GB and (b) orientation maps of UCR processed 90% deformed Al-2.5%Mg alloy

Upon further cold rolling to 90% reduction in thickness by the UCR route a lamellar structure sub-divided by extended boundaries parallel to the RD which is typical of heavily rolled fcc metals and alloys appears. Local shearing effect is also clearly visible in the GB map shown in Fig.4.28 (a). The quantitative analysis of the microtexture from the orientation map Fig.4.28 (b) shows abundance of Cu, S and  $B_S$  oriented regions in the 90% deformed material.



(a)



(b)

Fig.4.29: (a) (111) PF and (b) ODF of 90% deformed UCR processed Al-2.5%Mg alloy

Figure 4.29(a) shows the (111) PF of 90% deformed material. The PF appears typical of heavily deformed medium to high stacking fault energy material revealing a pure metal or copper type deformation texture characterized by the strong presence of the S,  $B_S$  and Cu components. From ODF (Fig.4.29(b)) from  $\phi_2 = 0^\circ$ ,  $45^\circ$  and  $65^\circ$  sections we can see that strong intensities are found around or near to the ideal Cu, S and  $B_S$  locations.

The microtexture measurement is also supported by bulk texture measurements by XRD. The PF (Fig.4.30 (a)) and ODF (Fig.4.30 (b)) determined by XRD show the development of typical pure metal or copper type texture in the bulk scale as well. Thus, excellent agreement is obtained between microtexture and bulk texture measurements.

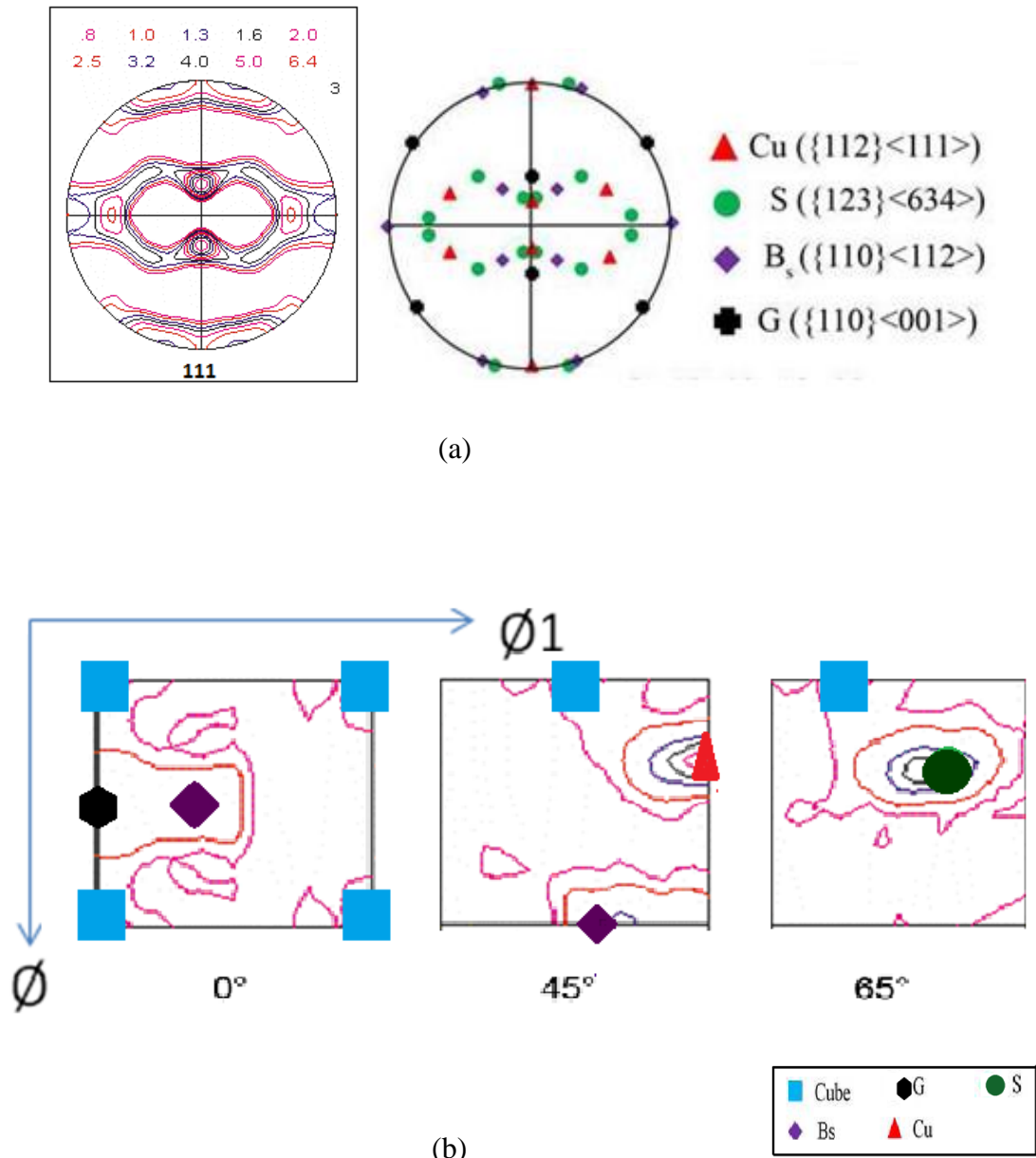


Fig.4.30: (a) (111) PF and (b) ODF of 90% deformed UCR processed Al-2.5%Mg alloy measured by XRD

### 4.2.3 Deformation by Cross Cold Rolling (CCR)

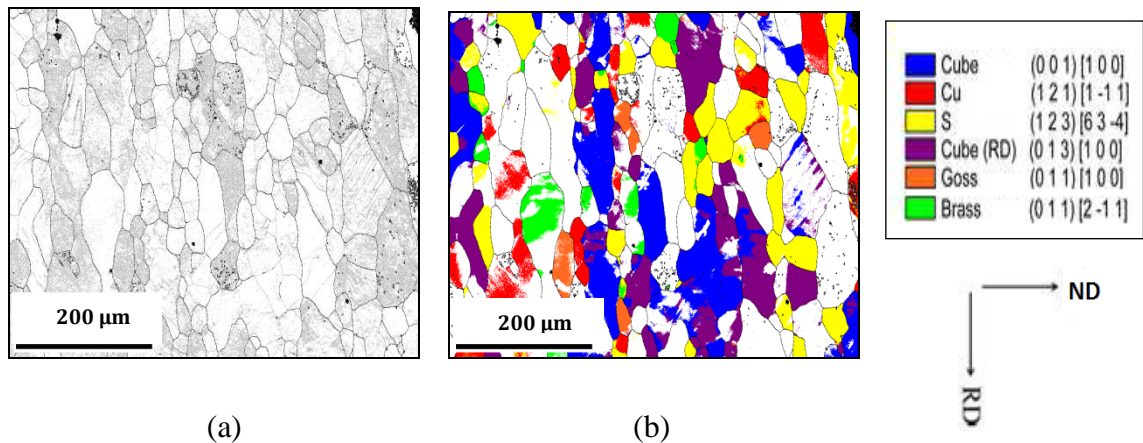
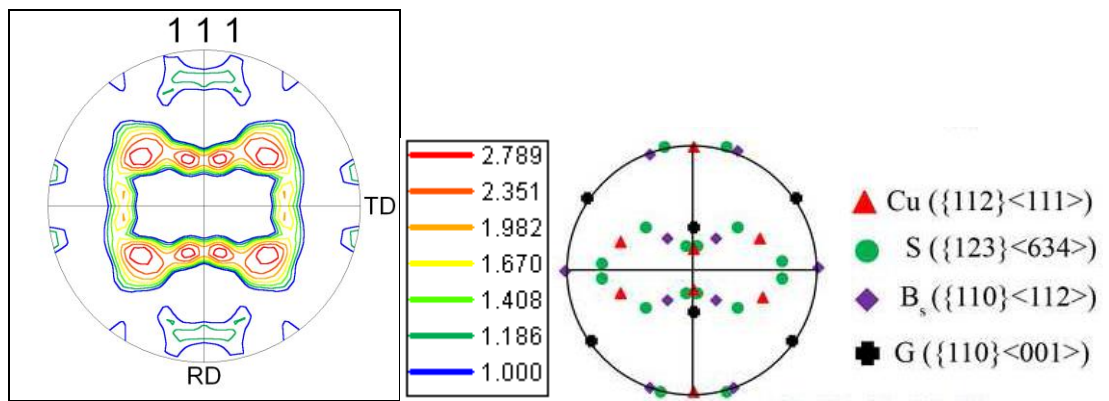


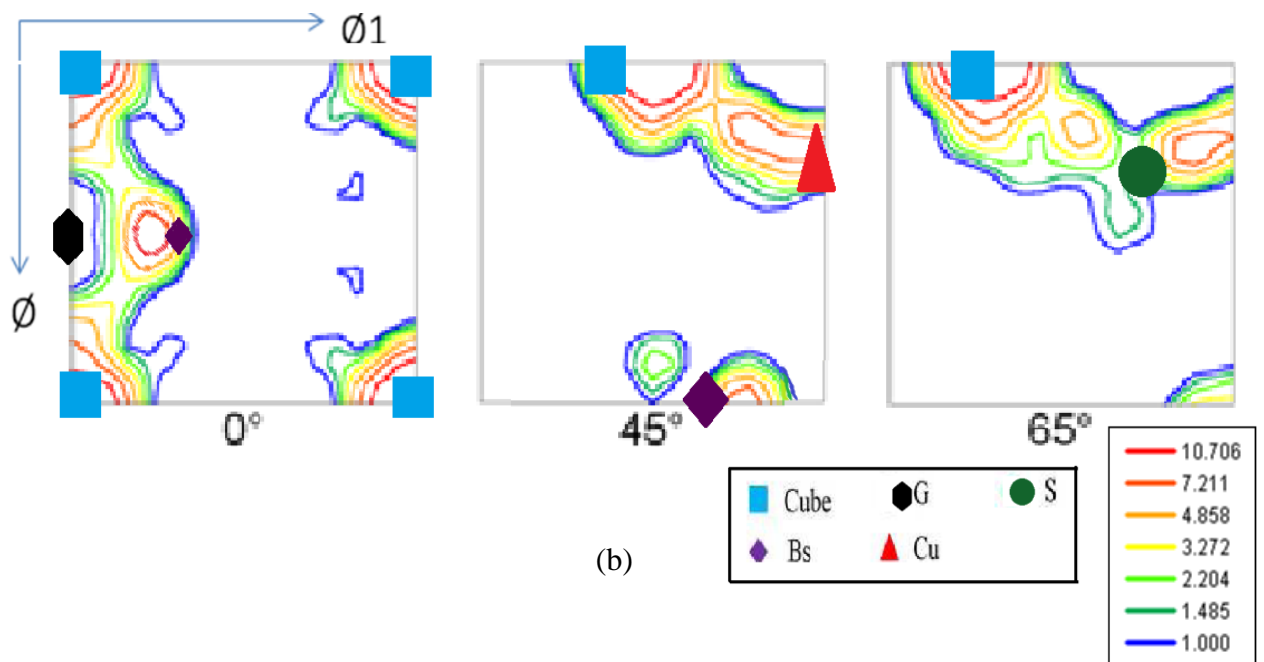
Fig.4.31: (a) GB and (b) orientation maps of CCR processed 20% Al-2.5%Mg alloy

Figure 4.31(a) shows the GB map of Al-2.5 Mg alloy following 20% reduction (by CCR route) in thickness. As like previous cases LAGB network can be clearly observed in the starting recrystallized grains after 20% deformation. The orientation map Fig.4.31 (b) reveals very similar texture components (C, Cu and S) which were observed in the starting recrystallized microstructure. This is also confirmed from the PF (Fig.4.32(a)) and the ODF (Fig.4.32(b)) sections.





(a)



(b)

Fig.4.32: (a) (111) PF and (b) the ODF of 20% deformed CCR processed Al-2.5%Mg alloy

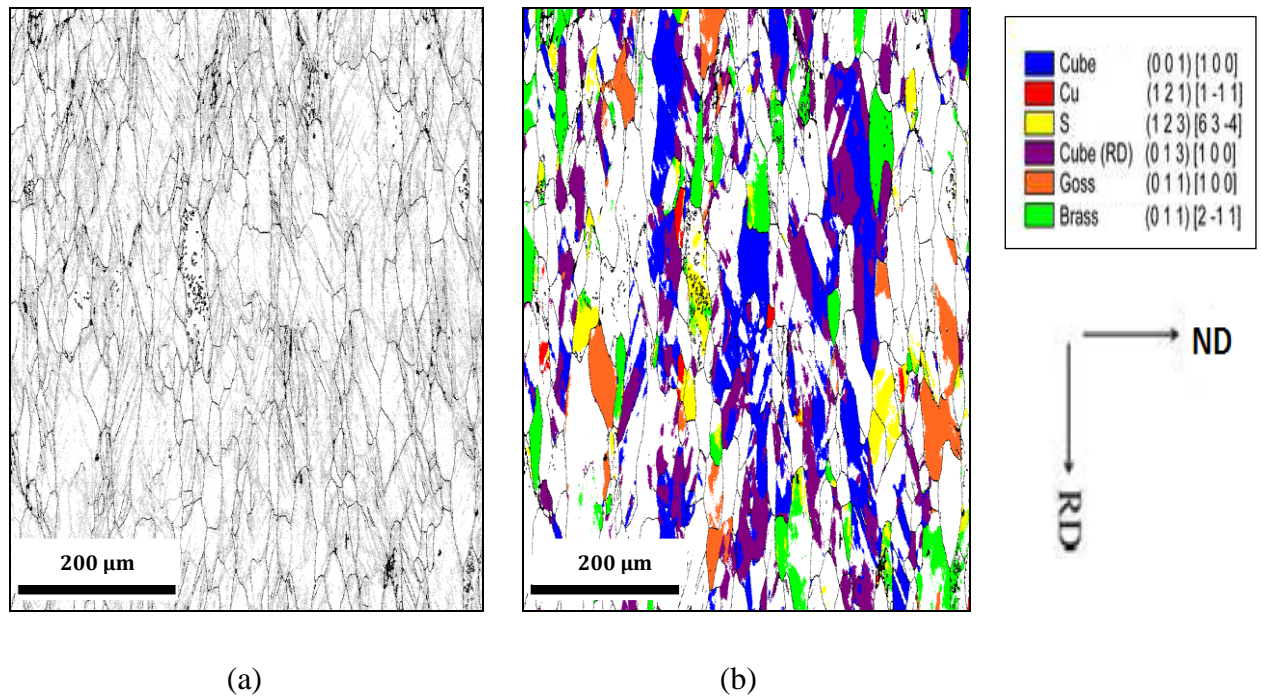
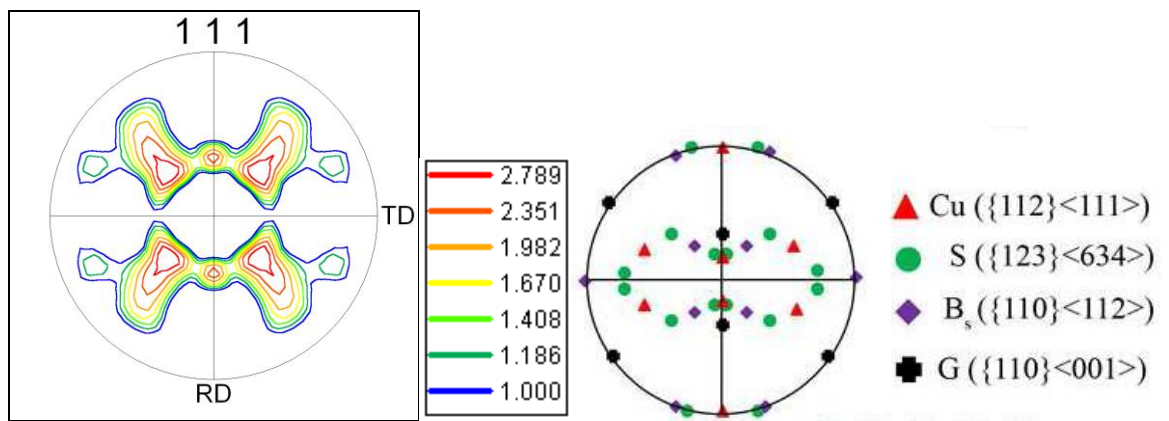
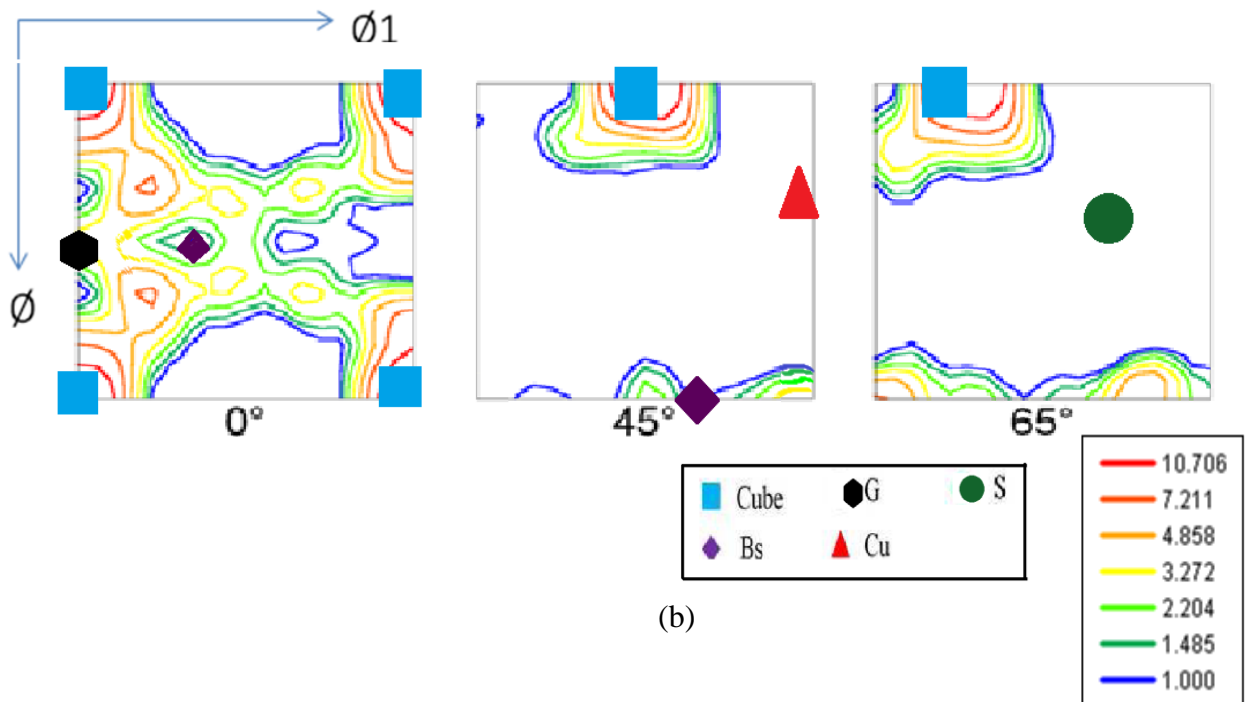


Fig.4.33: (a) GB and (b) orientation maps of CCR processed 40% deformed Al-2.5%Mg alloy

Figure 4.33(a) shows the GB map of the 40% deformed CCR processed material. Inside the deformed grains LAGB aligned to the RD could easily be noticed. The corresponding orientation map (Fig.4.33(b)) shows the presence of C orientation possibly inherited from the starting C oriented grains in the recrystallized microstructure. High volume fraction of non-rolling texture orientations could also be observed. The appearance of the (111) PF (Fig.4.34(a)) and ODF sections (Fig.4.34(b)) corroborate these observations Fig.4.34((a)-(b)).



(a)



(b)

Fig.4.34: (a) (111) PF and (b) ODF of 40% deformed CCR processed Al-2.5%Mg

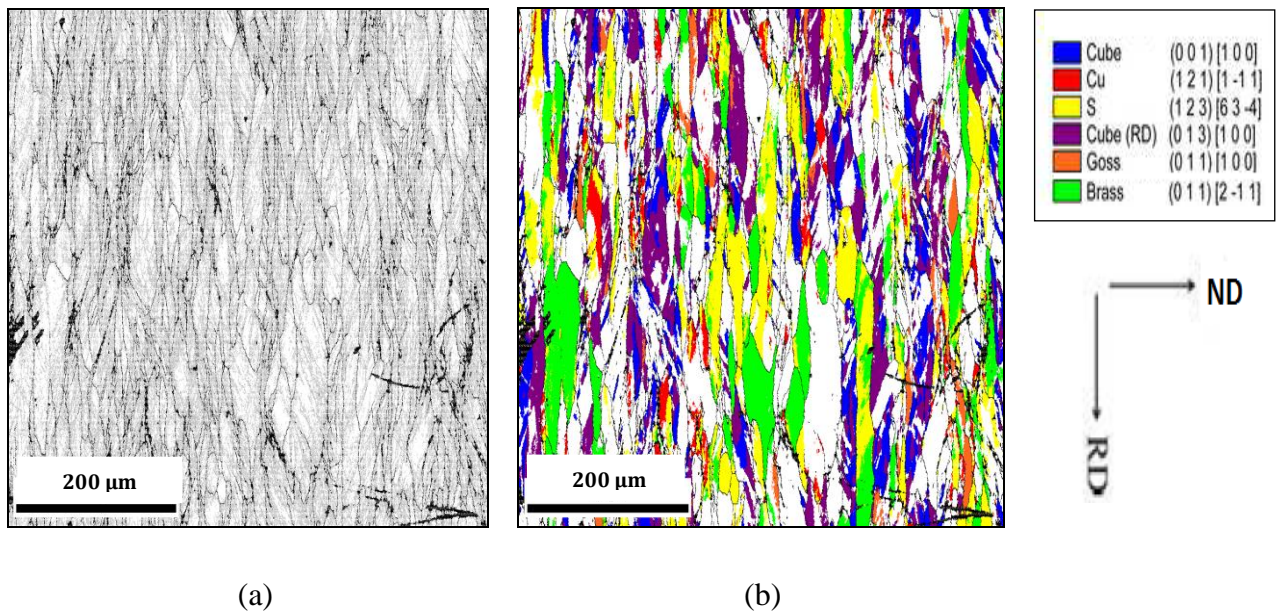
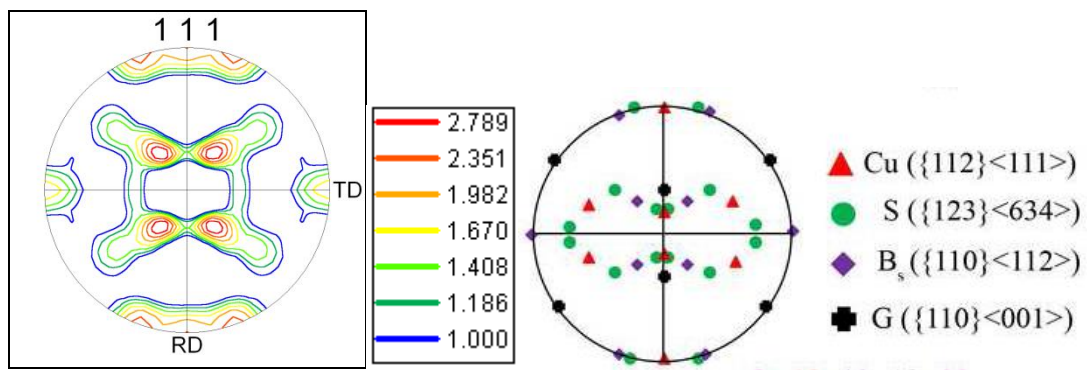
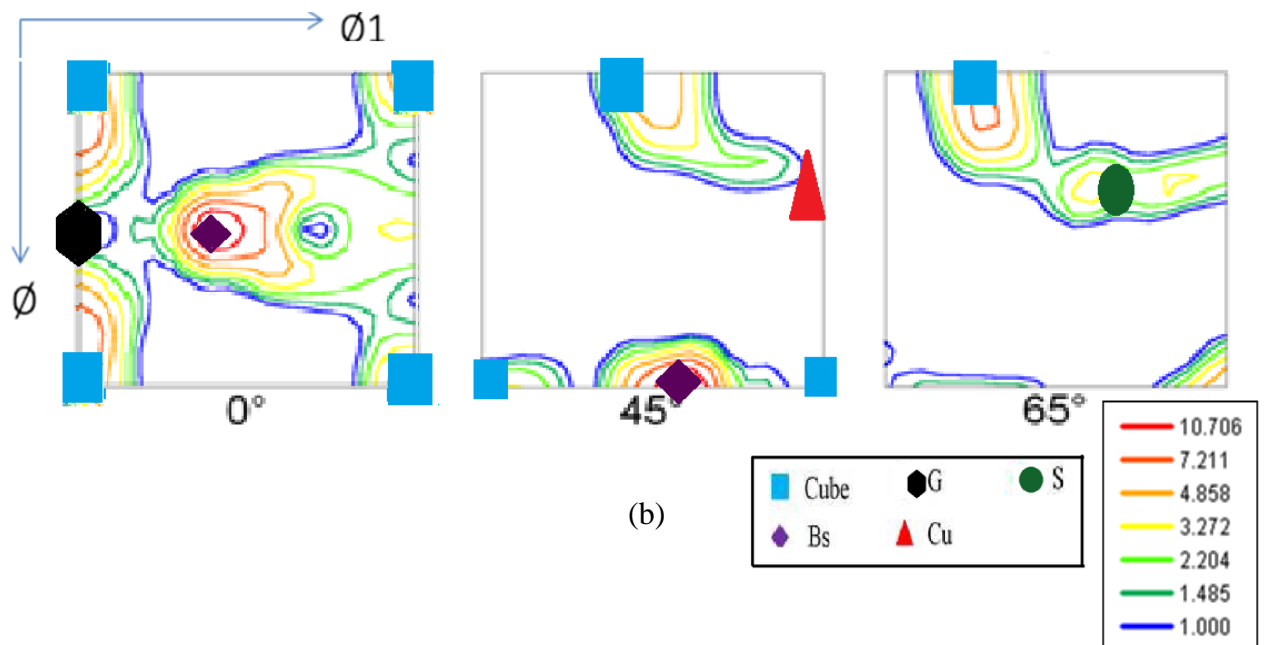


Fig.4.35: (a) GB and (b) orientation maps of CCR processed 60% deformed Al-2.5%Mg alloy

A lamellar structure sub-divided by HAGBs evolves after 60% deformation (Fig.4.35 (a)) although inside the elongated bands many LAGBs can be easily observed. The corresponding orientation map (Fig.4.35 (b)) shows profuse Bs, S, fragmented C and  $C_{RD}$  oriented regions. The PF also clearly show relative high intensity clustered around the ideal Bs location. The  $\varphi_2=0^\circ$  section show the spread of the C component around the  $\varphi_1$  axis which indicates the presence of the  $C_{RD}$  orientation in the microstructure



(a)



(b)

Fig.4.36: (a) (111) PF and (b) ODF of 60% deformed CCR processed Al-2.5%Mg

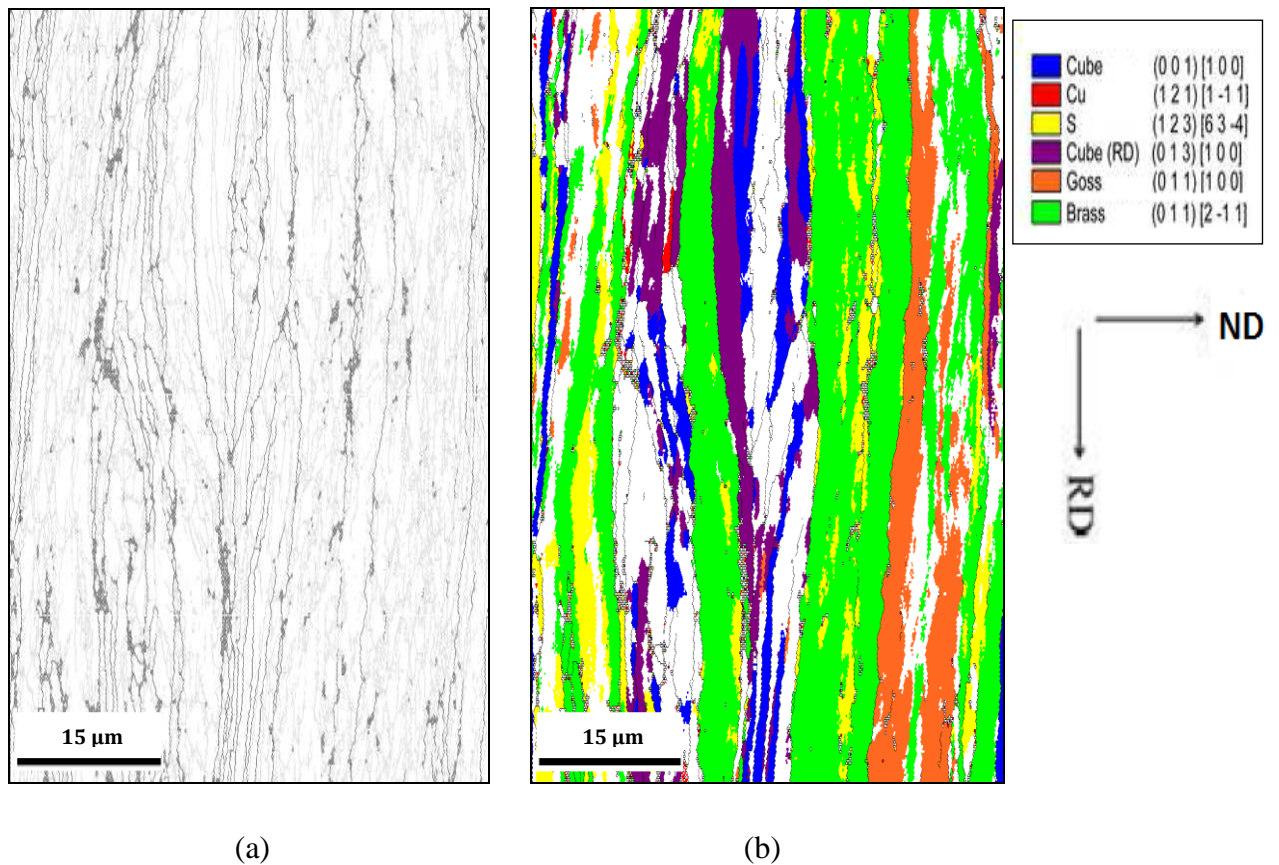
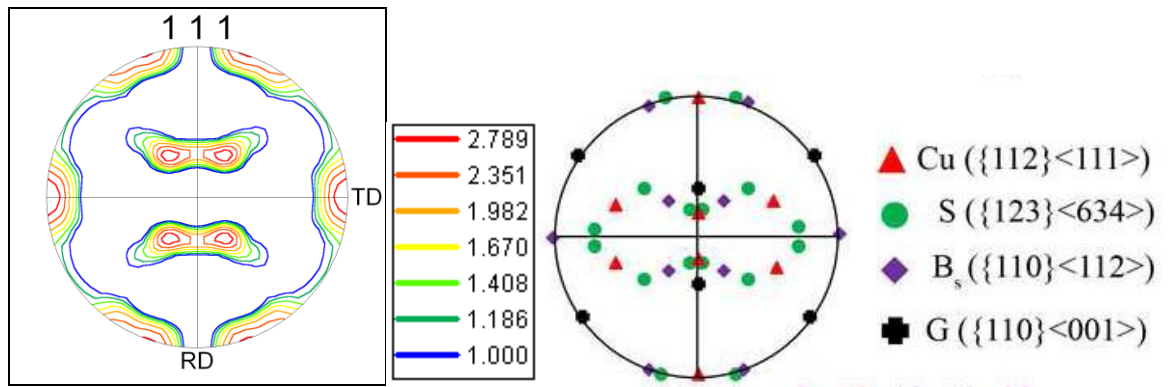
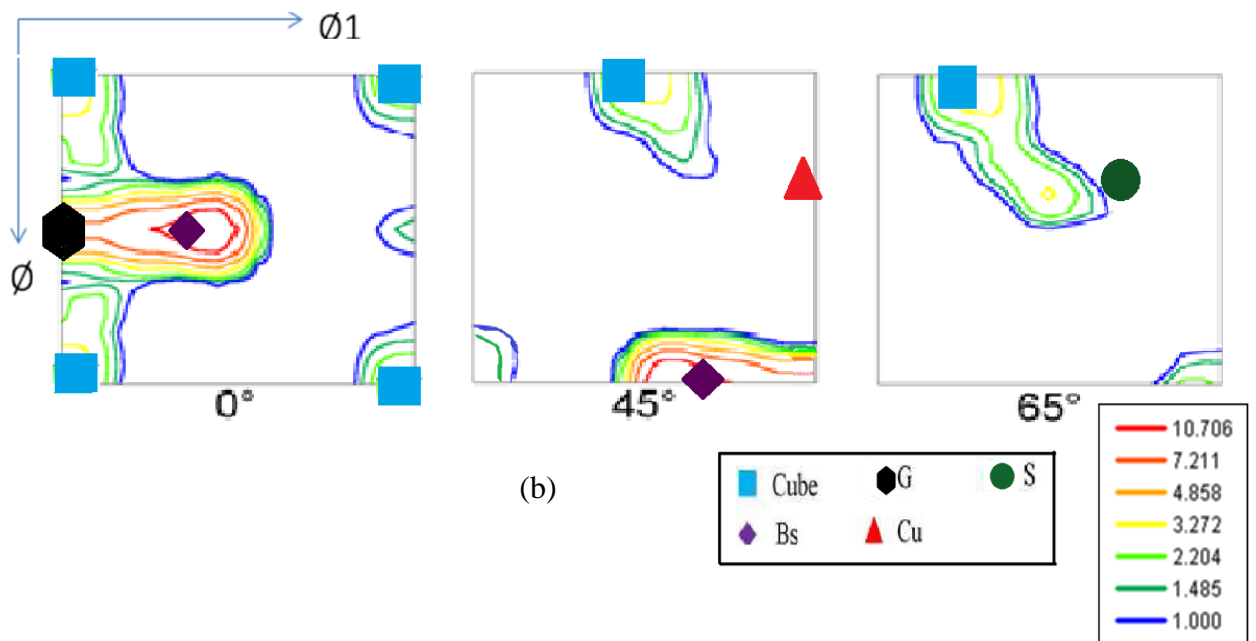


Fig.4.37: (a) GB and (b) orientation maps of CCR processed 90% deformed Al-2.5% Mg Alloy

Following 90% deformation by the CCR route a very clear lamellar structure evolves in the Al-2.5%Mg alloy (Fig.4.37 (a)). However, some elongated bands are found to be having much lesser thickness than some other neighbouring bands. The corresponding crystal orientation map (Fig.4.37 (b)) indicates very strong presence of the Bs orientation. The (111) PF (Fig.4.38 (a)) obtained from this region clearly reveal this fact. A close analysis of the  $\phi_2=0^\circ$  section of the ODF (Fig.4.38(b)) indicates that the intensity maxima associated with the Bs orientation is slightly shifted from the ideal Bs location along the axis  $\phi$  which indicates that the orientation is a ND-rotated Bs orientation ( $B_S^{ND}$ ) and can be described by the ideal orientation. .



(a)



(b)

Fig.4.38: (a) (111) PF and (b) ODF of 90% deformed CCR processed Al-2.5%Mg alloy

The (111) PF and ODF obtained from the bulk texture measurement by XRD is shown in Fig.4.39. Development of very strong  $B_s$  orientation is very clear from the appearance of the PF. The  $\phi_2=0^\circ$  section of the ODF indicates that the intensity of the  $B_s$  maxima is shifted from the ideal  $B_s$  location indicating the presence of a  $B_s^{ND}$  orientation. Excellent agreement between micro and bulk texture measurement can thus be easily noticed.

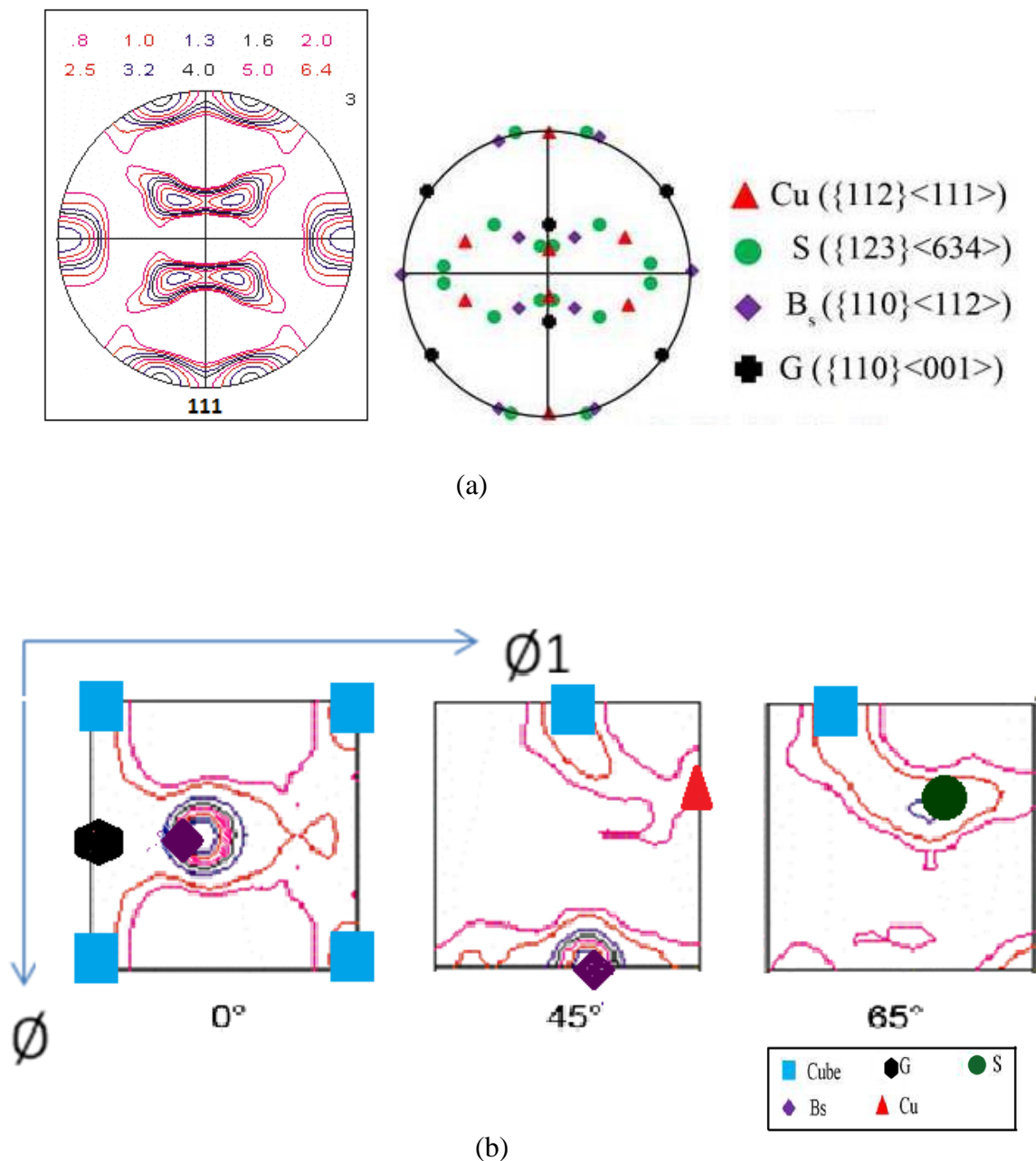


Fig.4.39: (a) (111) PF and (b) ODF of 90% deformed CCR processed Al-2.5%Mg alloy measured by XRD



#### 4.2.4 Evolution of Hardness Property

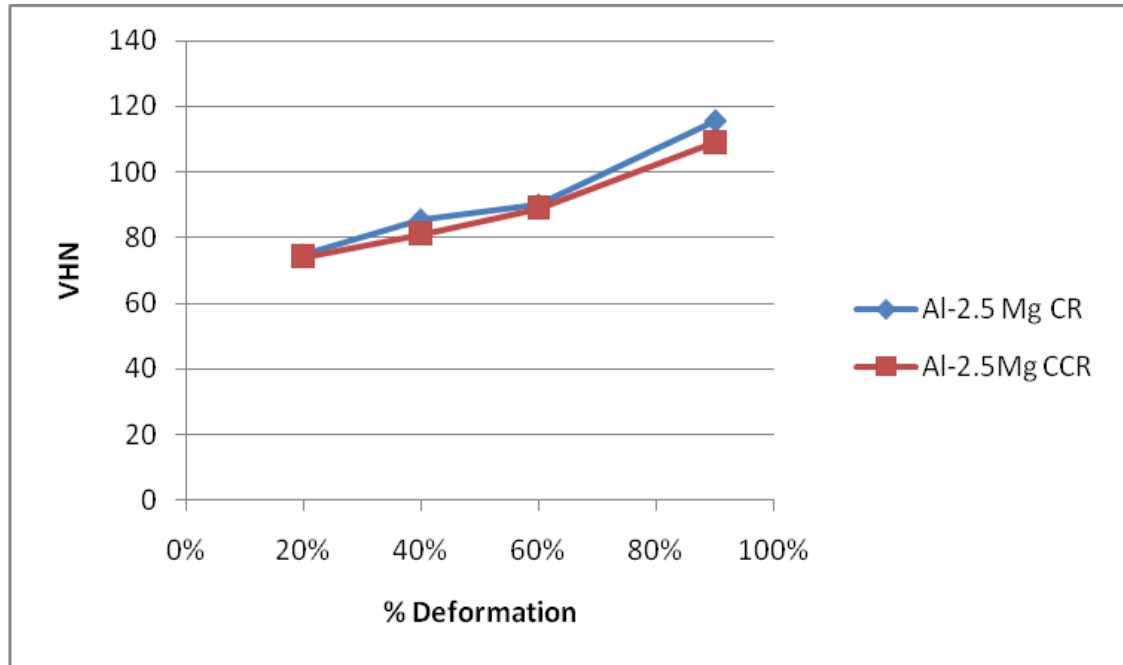


Fig.4.40: Evolution of hardness properties in UCR and CCR processed Al-2.5%Mg alloy

Hardness properties were determined at the RD-ND plane along the rolling direction. From Fig.4.40 it may be seen that hardness increases with increasing deformation. For 20%, 40% & 60% deformation level the hardness values of UCR and CCR processed materials appear quite comparable. However, for 90% deformed material we can observe the average hardness value of UCR processed Al-2.5%Mg alloy is decidedly greater than that of its CCR processed counterpart.

# Chapter 5

## Discussion

### 5.1 Effect of CCR processing on texture evolution

A major interest of the present work has been to understand the effect of CCR processing on the development of texture in the two experimental materials. For the sake of clarity the main observations pertaining to texture formation are summarized in Fig.5.1 and Fig. 5.2 which show the (111) pole figures obtained by XRD of differently processed materials and volume fraction of different texture components, namely, Cu, S and  $B_S$  obtained by EBSD, respectively. Figure 5.1(a)-(b) clearly shows the development of a pure metal or copper type deformation texture due to UCR processing in both the experimental materials characterized by the presence of strong Cu, S and  $B_S$  components (Fig.5.2). However, the deformation texture appears to be better developed in UCR processed Al-Mg alloy as compared to 4N-Al. The CCR processing leads to development of strong  $B_S$  component in the Al-Mg alloy at the expense of Cu and S components (refer to Fig.5.1(d) and Fig.5.2). The texture of CCR processed Al-Mg alloy is found very similar to the CCR processed texture of Al-Mn alloy[9] and other medium to high stacking fault energy fcc materials reported by different researchers[5,6,8,22,24].

In contrast, the  $B_S$  component increases only slightly after CCR processing in 4N-Al as compared to its UCR processed counterpart. The volume fraction of the  $B_S$  component in CCR processed 4N-Al is only 7% which is decidedly much lower than that in CCR processed Al-Mg alloy (~35%). A closer look at the  $\varphi_2=0^\circ$  section of the X-ray and EBSD measured ODFs reveal that the intensity associated with the  $B_S$  orientation is actually shifted through the  $\varphi_1$  axis and found at the location  $((\varphi_1, \varphi, \varphi_2)=(47^\circ, 45^\circ, 0^\circ))$  corresponding to the ND-rotated  $B_S$  orientation ( $B_S^{ND}$ ) (011)[17 -13 13]. When this orientation is plugged in the orientation map of the 90% CCR processed material the combined volume fraction of  $B_S$  and  $B_S^{ND}$  (highlighted in pale green) is found to be ~17% which is still much lower than the  $B_S$  fraction in CCR processed Al-Mg alloy (~35%).

The development of  $B_S$  texture during deformation processing may be understood by analyzing the stability of different orientations [25,26]. The stability of any orientation during deformation processing is determined from two factors, namely, the rotation field ( $\dot{R}$ ) which is the time derivative of the three Euler angles ( $\dot{R} = \dot{\phi}_1, \dot{\phi}, \dot{\phi}_2$ ) and the divergence of the rotation field ( $div \dot{R} = \frac{\partial \dot{\phi}_1}{\partial \varphi} + \frac{\partial \dot{\phi}}{\partial \varphi} + \frac{\partial \dot{\phi}_2}{\partial \varphi}$ ). For an orientation to be stable two conditions, namely,  $\dot{R} = 0$  and  $div \dot{R} < 0$ . The theoretical calculations of Hong et al [7] predict that amongst different texture components the  $\{011\}\langle 1-11 \rangle$  (which is basically ND rotated  $B_S$  orientation) would be stable under cross-rolling due to its higher inverse rotation rate and large negative divergence. The grains with orientations along the  $\alpha$ -fiber will rotate to the  $B_S$  orientation (stable orientation during unidirectional rolling) and then will further rotate away to the

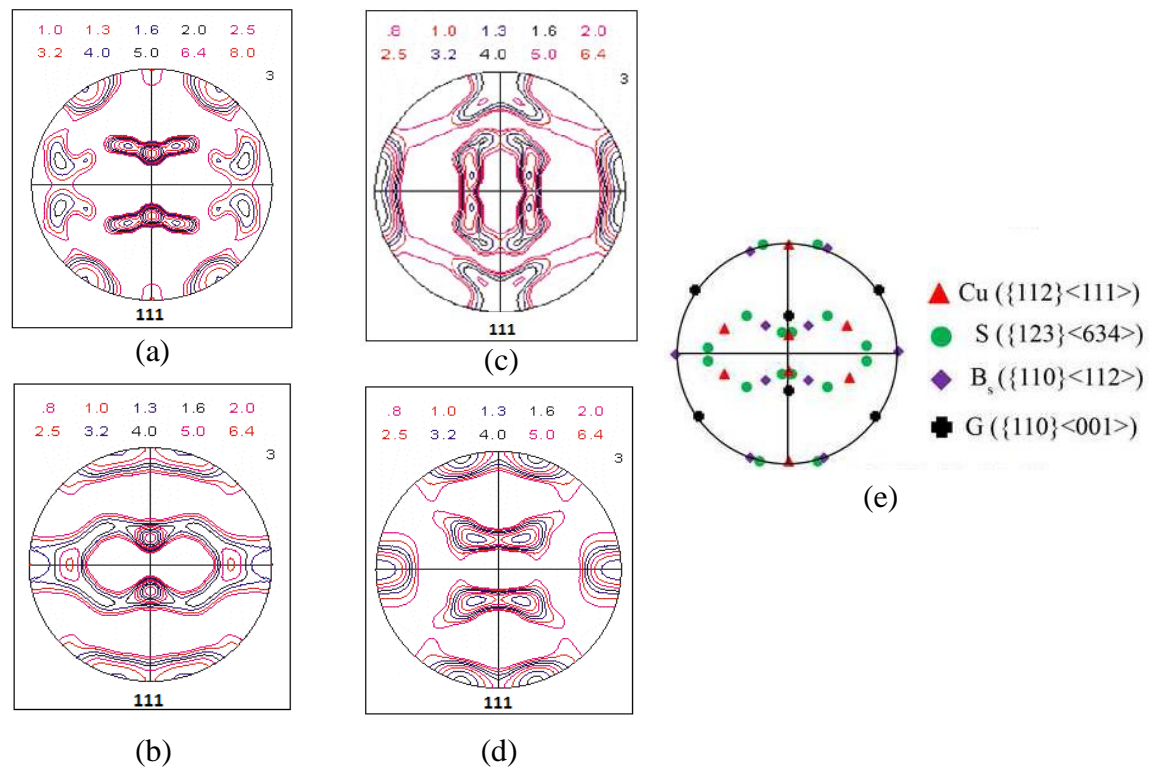


Fig. 5.1: (111) pole figures of UCR processed (a) 4N-Al and (b) Al-Mg; CCR processed (c) 4N-Al and (d) Al-Mg. The ideal location of the typical deformation texture components are shown in Fig.5.1 (e).

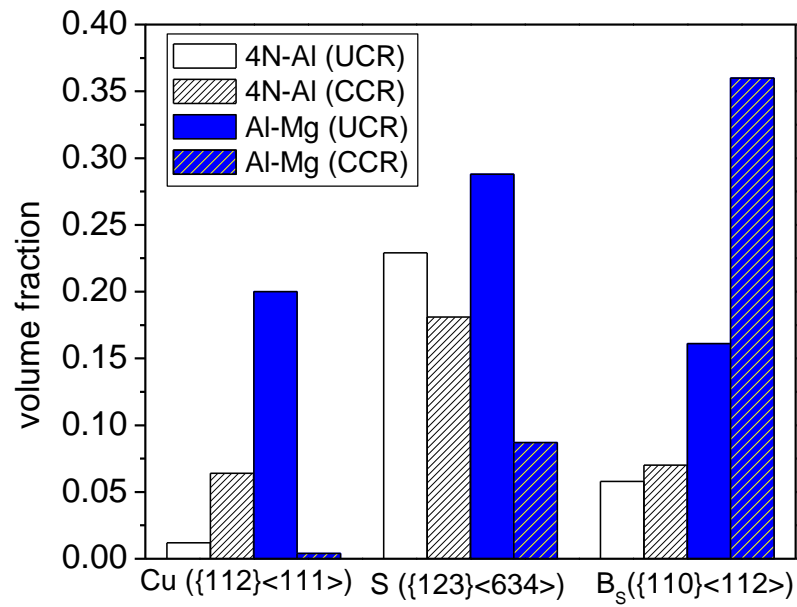


Fig.5.2: Change in volume fraction of different texture components with increasing strain in 4N-Al and Al-Mg during (a) UCR and (b) CCR processing (Calculated from microtexture measurement from EBSD scan of deformed 4N Al sample at various thickness reductions).

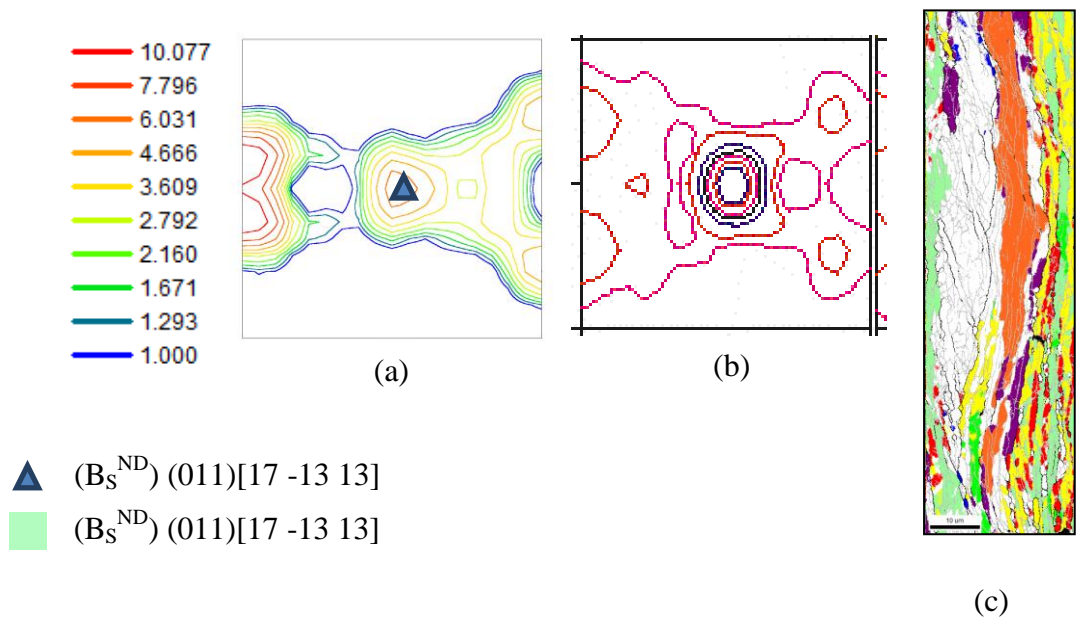


Fig.5.3:  $\Phi_2=0^\circ$  section of the ODF of 90% deformed CCR processed 4N-Al measured by (a) EBSD, (b) XRD; (c) is the corresponding orientation map.

$\{011\}\langle 1\bar{1}1\rangle$  orientation when the direction of rolling is changed by  $90^\circ$  around the ND, thus, oscillating between the  $B_S$  and rotated brass orientation  $\{011\}\langle 1-11\rangle$  which would be the two dynamically stable end orientations in CCR processed materials.

It may be observed that while  $B_S$  component is stronger in Al-Mg alloy and also found almost near the ideal  $B_S$  location for 4N-Al stronger  $B_S^{ND}$  component is observed and the combined volume fraction of  $B_S$  and  $B_S^{ND}$  components is lower than the  $B_S$  component in Al-Mg alloy. One possible reason for the observed difference could be due to the solute hardening in Al-Mg due to the presence of Mg in solid solution. Due to the increased solid solution hardening the grain rotation during CCR processing should be more difficult in Al-Mg alloy. On the other hand this grain rotation is much easier in 4N-Al. Therefore, during the cross rolling the grains of the  $\alpha$ -fiber can first rotate to the  $B_S$  orientation and then can further rotate away which might possibly be the reason for the observed differences. An increased volume fraction of the  $B_S^{ND}$  component in CCR processed 4N-Al appears to be consistent with this fact.

## 5.2 Effect of CCR processing on microstructure evolution

It may be observed clearly from the present study that 4N-Al and Al-Mg alloy gradually develop lamellar type deformation microstructure following heavy deformation by different rolling routes. This is clearly confirmed from the GB maps of 90% deformed UCR and CCR processed 4N-Al (Fig.4.8 and Fig. 4.17) and Al-Mg (Fig.4.28 and Fig.4.37). The development of such lamellar type structure in heavily deformed materials has been studied extensively and well documented in literature which agrees quite well with the present observations.

In order to clearly elucidate the impact of heavy deformation by CCR processing on the evolution of microstructure in the two materials it may be useful to look at the evolution of key structural parameters to describe lamellar type deformation structure such as HAGB spacing along the ND ( $d_{HAGB}^{ND}$ ), HAGB fraction ( $f_{HAGB}$ ) and average misorientation angle ( $\theta_{avg}$ ) which are obtained from the relevant GB maps in Chapter 4 and presented in Fig.5.4.

The initial decrease in the HAGB fraction which is observed irrespective of materials and processing routes is due to the development of cell structure composed of LAGB network inside the starting recrystallized grains. This effect is of course much more drastic in the case of Al-Mg alloy. Beyond 20% deformation the HAGB fraction tends to increase in all cases up to 90% thickness reduction i.e. the maximum strain level studied in this work except for the 4N-Al CCR for which, very interestingly, the HAGB fraction continues to decrease up to 60% reduction in thickness and then increases beyond this deformation level. The HAGB fraction of the 90% deformed UCR and CCR processed Al-Mg alloy does not differ to any significant extent (~0.24 and 0.26 respectively i.e. an increase of only 8.33% in CCR processed material). However, wide difference in the HAGB fraction is observed for the 90% deformed UCR and CCR processed 4N-Al (0.32 and 0.20, respectively. i.e. an increase of more than 50% in UCR processed material as compared to the CCR processed material). These differences in HAGB fraction is also reflected in the evolution of average misorientation angle (Fig.5.4(b))and HAGB spacing values of differently processed materials. The average misorientation angle and HAGB spacing values in the UCR and CCR processed Al-Mg alloy appear very similar but wide difference is observed in the case of two differently processed 4N-Al materials. It is thus very apparent that CCR processing has a much pronounced effect on microstructural evolution in 4N-Al as compared to the Al-Mg alloy.

The microstructure of 90% deformed UCR and CCR processed microstructure indicates some important differences. As already pointed out very clear sub-grain structure was observed in the UCR processed material indicating pronounced dynamic recovery. The dynamic recovery results in the annihilation of dislocations and decrease in the fraction of LAGBs which quite rightly justify both the increase in HAGB fraction and appearance of a (sub)grain structure. However, such a clear sub-grain structure is not established from the corresponding GB map. It appears at this stage that dynamic recovery is restricted during CCR processing leading to lesser annihilation of dislocations and consequently lower HAGB fraction. However, the reasons for decreased dynamic recovery during CCR processing need to be investigated further.

Dynamic recovery is much easier in 4N-Al as compared Al-Mg. It is well known that recovery is restricted in Al-Mg alloy due to the presence of Mg as solute[27]. As a result CCR processing seems to have little impact in microstructural evolution which is clearly established

from the very similar values of the key microstructural parameters of the UCR and CCR processed heavily deformed Al-Mg alloy.

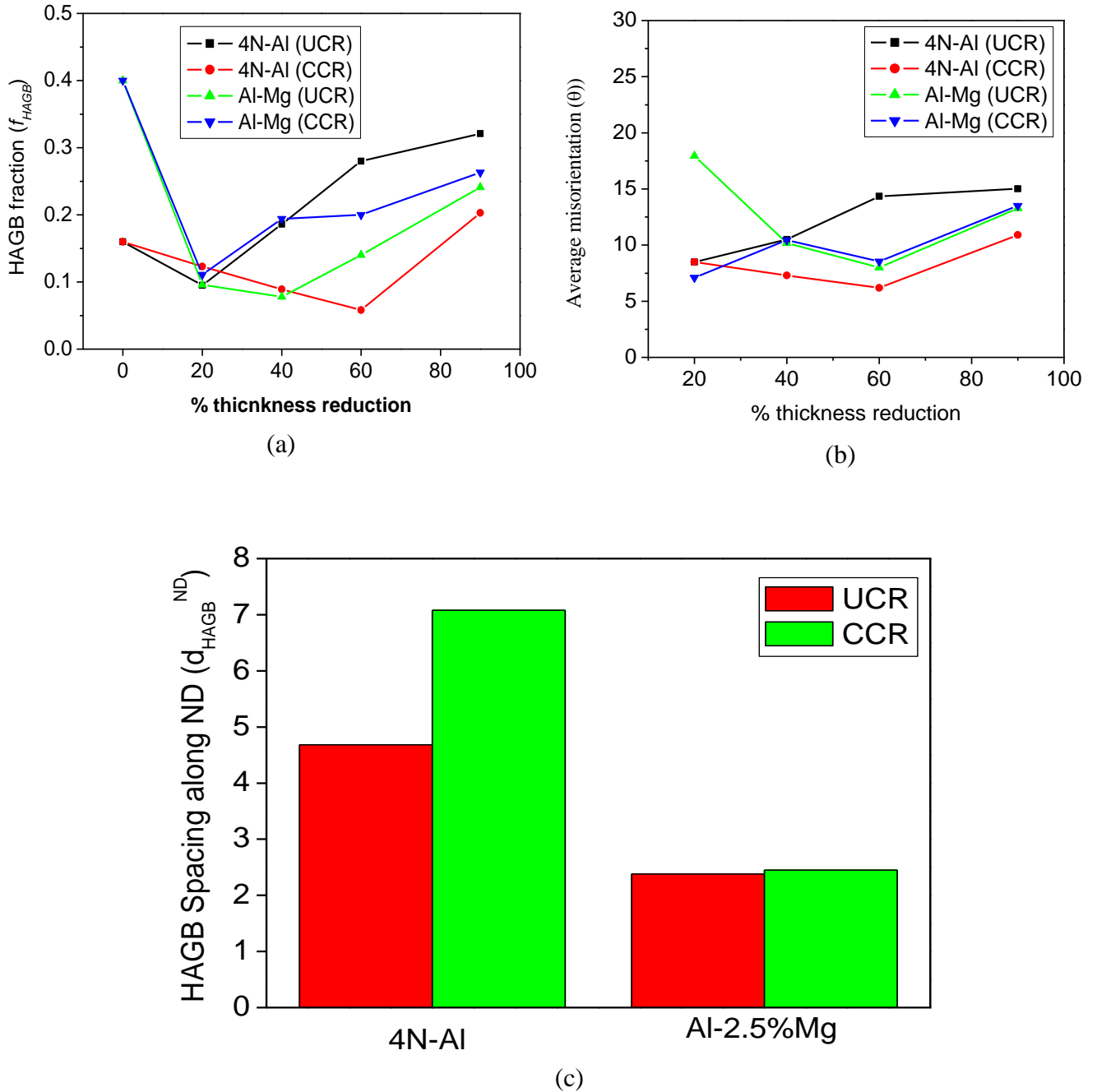


Fig.5.4: Evolution of key structural parameters; (a) HAGB fraction ( $f_{HAGB}$ ), (b) average misorientation angle ( $\theta$ ) and (c) HAGB spacing along the ND ( $d_{ND}^{HAGB}$ ).

## **5.3 Evolution of hardness properties**

The hardness values of Al-Mg alloy processed by two different routes do not differ significantly. In heavily deformed condition the hardness value of UCR processed material is found slightly more than CCR processed material which is in very good agreement with the slightly finer microstructure (larger HAGB fraction and lower HAGB spacing) in the UCR processed material as compared to its CCR processed counterpart (Fig.4.42).

The hardness values of 90% deformed 4N-Al shows different behavior. The UCR processed material shows consistently greater hardness values at all deformation level. The lower hardness value in the 90% deformed CCR processed 4N-Al agrees well with the more recovered structure observed for this material. It appears that dynamic recovery in the CCR processed material leads to softening by dislocation annihilation resulting in lower hardness values as compared to its UCR processed counterpart (Fig.4.20).

## **5.4 Future work**

### **5.4 Future work**

- TEM observation of differently processed material to gain better understanding of the deformation microstructure.
- Tensile testing of differently processed materials to correlate the hardness properties with tensile deformation behavior.



# Chapter 6

## Summary and Conclusions

The major findings of the present work may be summarized as:

- UCR processing leads to a pure metal type deformation texture characterized by strong Cu ( $\{112\}\langle 111\rangle$ ), S ( $\{123\}\langle 634\rangle$ ) and  $B_S(\{110\}\langle 112\rangle)$  components in 4N-Al and Al-Mg alloys.
- Al-Mg alloy develops a much stronger  $B_S$  component after CCR processing than its UCR processed counterpart.
- In CCR process texture of 4N-Al  $B_S$  and  $B_S^{ND}(011)[17 -13 13]$  components are observed. The combined volume fraction of these two components is, however, much smaller than the volume fraction of the  $B_S$  component in Al-Mg.
- Evolution of a lamellar type deformation microstructure is observed in all materials irrespective of the processing route.
- The CCR processed 4N-Al shows much pronounced dynamic recovery. The reasons for restricted dynamic recovery in UCR processed 4N-Al needs to be investigated further.
- The CCR processing does not affect the microstructural development of Al-Mg alloy significantly as established by the values of the key structural parameters of differently processed heavily deformed materials. This seems to originate from the absence of dynamic recovery in Al-Mg alloy due to the presence of Mg as solute.
- The hardness values of heavily deformed Al-Mg processed by different routes do not differ appreciably which is consistent with the very similar values of their microstructural parameters.
- UCR processed 4N-Al show consistently higher values than its CCR processed counterpart presumably due to less dynamic recovery in the former material.
- Importantly, UCR processing appears to have more pronounced effect on microstructure, texture and properties of materials with strong tendency for dynamic recovery.

- The above observations support the basic idea based up on which the present research work has been initiated.
- Further studies based on TEM observations and tensile deformation behavior should clarify the structure-texture-property relationship in CCR processed 4N-Al.

# References

- [1] J. Hirsch, K. Lücke, *Acta Metallurgica*, 36 (1988) 2863-2882.
- [2] J. Hirsch, K. Lücke, *Acta Metallurgica*, 36 (1988) 2883-2904.
- [3] J. Hirsch, K. Lücke, M. Hatherly, *Acta Metallurgica*, 36 (1988) 2905-2927.
- [4] P.P. Bhattacharjee, R.K. Ray, N. Tsuji, *Acta Materialia*, 57 (2009) 2166-2179.
- [5] S. Suwas, A.K. Singh, K.N. Rao, T. Singh, *Zeitschrift Fur Metallkunde*, 94 (2003) 1313-1319.
- [6] S. Suwas, A.K. Singh, *Materials Science and Engineering a-Structural Materials Properties Microstructure and Processing*, 356 (2003) 368-371.
- [7] S.H. Hong, D.N. Lee, *Journal of Engineering Materials and Technology, Transactions of the ASME*, 124 (2002) 13-22.
- [8] A. Merlini, P.A. Beck, *Acta Metallurgica*, 1 (1953) 598-606.
- [9] A. Bocker, H. Klein, H.J. Bunge, *Textures and Microstructures*, 12 (1990) 155-174.
- [10] M.Y. Huh, S.Y. Cho, O. Engler, *Materials Science and Engineering: A*, 315 (2001) 35-46.
- [11] S.H. Kim, H.G. Kang, M.Y. Huh, O. Engler, *Materials Science and Engineering: A*, 508 (2009) 121-128.
- [12] X.Y. Kong, W.C. Liu, J. Li, H. Yuan, *Journal of Alloys and Compounds*, 491 (2010) 301-307.
- [13] W. Liu, X. Li, X. Meng, *Scripta Materialia*, 60 (2009) 768-771.
- [14] C. Mondal, A.K. Singh, A.K. Mukhopadhyay, K. Chattopadhyay, *Scripta Materialia*, 64 (2011) 446-449.
- [15] J.G. Sevillano, P. Vanhoutte, E. Aernoudt, *Progress in Materials Science*, 25 (1980) 69-412.
- [16] I. Barker, N. Hansen, B. Ralph, *Materials Science and Engineering a-Structural Materials Properties Microstructure and Processing*, 113 (1989) 449-454.
- [17] N. Hansen, *Materials Science and Technology*, 6 (1990) 1039-1047.
- [18] N. Hansen, *Scripta Metallurgica Et Materialia*, 27 (1992) 1447-1452.
- [19] B. Bay, N. Hansen, D.A. Hughes, D. Kuhlmannwilsdorf, *Acta Metallurgica Et Materialia*, 40 (1992) 205-219.

- [20] D.A. Hughes, N. Hansen, *Metallurgical Transactions a-Physical Metallurgy and Materials Science*, 24 (1993) 2021-2037.
- [21] T. Leffers, R.K. Ray, *Progress in Materials Science*, 54 (2009) 351-396.
- [22] N.P. Gurao, S. Sethuraman, S. Suwas, *Materials Science and Engineering A*, 528 (2011) 7739-7750.
- [23] S. Suwas, A.K. Singh, K.N. Rao, T. Singh, *Zeitschrift fuer Metallkunde/Materials Research and Advanced Techniques*, 93 (2002) 918-927.
- [24] T. Öztürk, *Scripta Metallurgica*, 22 (1988) 1611-1616.
- [25] J. Savoie, J.J. Jonas, *Acta Metallurgica Et Materialia*, 42 (1994) 4101-4116.
- [26] L.S. Toth, J.J. Jonas, D. Daniel, R.K. Ray, *Metallurgical Transactions a-Physical Metallurgy and Materials Science*, 21 (1990) 2985-3000.
- [27] F.J. Humphreys, M. Hatherly, in: *Recrystallization and Related Annealing Phenomena (Second Edition)*, Elsevier, Oxford, 2004, p.173.